CrossMark

CEERS Epoch 1 NIRCam Imaging: Reduction Methods and Simulations Enabling Early JWST Science Results

Micaela B. Bagley[1] , Steven L. Finkelstein[1] , Anton M. Koekemoer[2] , Henry C. Ferguson[2] , Pablo Arrabal Haro[3] ,
Mark Dickinson[3] , Jeyhan S. Kartaltepe[4] , Casey Papovich[5,6] , Pablo G. Pérez-González[7] , Nor Pirzkal[8] ,
Rachel S. Somerville[9] , Christopher N. A. Willmer[10] , Guang Yang[11,12] , L. Y. Aaron Yung[13,32] , Adriano Fontana[14] ,
Andrea Grazian[15] , Norman A. Grogin[2] , Michaela Hirschmann[16] , Lisa J. Kewley[17] , Allison Kirkpatrick[18] ,
Dale D. Kocevski[19] , Jennifer M. Lotz[20] , Aubrey Medrano[21] , Alexa M. Morales[1] , Laura Pentericci[14] ,
Swara Ravindranath[2] , Jonathan R. Trump[22] , Stephen M. Wilkins[23,24] , Antonello Calabrò[14] , M. C. Cooper[25] ,
Luca Costantin[26] , Alexander de la Vega[27] , Bryan Hilbert[2] , Taylor A. Hutchison[13,31] , Rebecca L. Larson[1,32] ,
Ray A. Lucas[2] , Elizabeth J. McGrath[19] , Russell Ryan[2] , Xin Wang[28,29] , and Stijn Wuyts[30]
[1] Department of Astronomy, The University of Texas at Austin, Austin, TX 78712, USA; mbagley@utexas.edu
[2] Space Telescope Science Institute, 3700 San Martin Drive, Baltimore, MD 21218, USA
[3] NSF's National Optical-Infrared Astronomy Research Laboratory, 950 N. Cherry Ave., Tucson, AZ 85719, USA
[4] Laboratory for Multiwavelength Astrophysics, School of Physics and Astronomy, Rochester Institute of Technology, 84 Lomb Memorial Drive, Rochester, NY 14623, USA
[5] Department of Physics and Astronomy, Texas A&M University, College Station, TX, 77843-4242 USA
[6] George P. and Cynthia Woods Mitchell Institute for Fundamental Physics and Astronomy, Texas A&M University, College Station, TX 77843-4242 USA
[7] Centro de Astrobiología (CAB), CSIC-INTA, Ctra. de Ajalvir km 4, Torrejón de Ardoz, E-28850, Madrid, Spain
[8] ESA/AURA Space Telescope Science Institute, USA
[9] Center for Computational Astrophysics, Flatiron Institute, 162 5th Avenue, New York, NY, 10010, USA
[10] Steward Observatory, University of Arizona, 933 N. Cherry Ave., Tucson, AZ, 85721, USA
[11] Kapteyn Astronomical Institute, University of Groningen, P.O. Box 800, 9700 AV Groningen, The Netherlands
[12] SRON Netherlands Institute for Space Research, Postbus 800, 9700 AV Groningen, The Netherlands
[13] Astrophysics Science Division, NASA Goddard Space Flight Center, 8800 Greenbelt Rd., Greenbelt, MD 20771, USA
[14] INAF—Osservatorio Astronomico di Roma, via di Frascati 33, I-00078 Monte Porzio Catone, Italy
[15] INAF—Osservatorio Astronomico di Padova, Vicolo dell'Osservatorio 5, I-35122, Padova, Italy
[16] Institute of Physics, Laboratory of Galaxy Evolution, Ecole Polytechnique Fdrale de Lausanne (EPFL), Observatoire de Sauverny, 1290 Versoix, Switzerland
[17] Center for Astrophysics | Harvard & Smithsonian, 60 Garden Street, Cambridge, MA 02138, USA
[18] Department of Physics and Astronomy, University of Kansas, Lawrence, KS 66045, USA
[19] Department of Physics and Astronomy, Colby College, Waterville, ME 04901, USA
[20] Gemini Observatory/NSF's National Optical-Infrared Astronomy Research Laboratory, 950 N. Cherry Ave., Tucson, AZ 85719, USA
[21] University of Massachusetts Amherst, 710 North Pleasant Street, Amherst, MA 01003-9305, USA
[22] Department of Physics, 196 Auditorium Road, Unit 3046, University of Connecticut, Storrs, CT 06269, USA
[23] Astronomy Centre, University of Sussex, Falmer, Brighton BN1 9QH, UK
[24] Institute of Space Sciences and Astronomy, University of Malta, Msida MSD 2080, Malta
[25] Department of Physics & Astronomy, University of California, Irvine, 4129 Reines Hall, Irvine, CA 92697, USA
[26] Centro de Astrobiología (CSIC-INTA), Ctra de Ajalvir km 4, Torrejón de Ardoz, E-28850, Madrid, Spain
[27] Department of Physics and Astronomy, University of California, 900 University Ave., Riverside, CA 92521, USA
[28] School of Astronomy and Space Science, University of Chinese Academy of Sciences (UCAS), Beijing 100049, People's Republic of China
[29] National Astronomical Observatories, Chinese Academy of Sciences, Beijing 100101, People's Republic of China
[30] Department of Physics, University of Bath, Claverton Down, Bath BA2 7AY, UK

Abstract

We present the data release and data reduction process for the Epoch 1 NIRCam observations for the Cosmic Evolution Early Release Science Survey (CEERS). These data consist of NIRCam imaging in six broadband filters (F115W, F150W, F200W, F277W, F356W and F444W) and one medium-band filter (F410M) over four pointings, obtained in parallel with primary CEERS MIRI observations. We reduced the NIRCam imaging with the JWST Calibration Pipeline, with custom modifications and reduction steps designed to address additional features and challenges with the data. Here we provide a detailed description of each step in our reduction and a discussion of future expected improvements. Our reduction process includes corrections for known prelaunch issues such as $1/f$ noise, as well as in-flight issues including snowballs, wisps, and astrometric alignment. Many of our custom reduction processes were first developed with prelaunch simulated NIRCam imaging over the full 10 CEERS NIRCam pointings. We present a description of the creation and reduction of this simulated data set in the Appendix. We provide mosaics of the real images in a public release, as well as our reduction scripts with detailed explanations to allow users to reproduce our final data products. These represent one of the first official public data

1

sets released from the Directors Discretionary Early Release Science (DD-ERS) program.

Unified Astronomy Thesaurus concepts: Near infrared astronomy (1093); Direct imaging (387); Astronomy data reduction (1861)

1. Introduction

The Directors Discretionary Early Release Science (DD-ERS) programs are providing the community with early and efficient demonstrations of the capabilities of JWST (Gardner et al. 2006). These public programs are designed to test multiple instruments and observing modes, and the teams have committed to sharing data products, tools and software, simulations, and documentation before the JWST Cycle 2 call for proposals. The 13 ERS programs cover a wide range of science topics and together have provided a wealth of information about early JWST performance and calibration.

Among these programs, the Cosmic Evolution Early Release Science Survey (CEERS; ERS 1345, PI: S Finkelstein) is obtaining imaging and spectroscopy of the Extended Groth Strip (EGS) Hubble Space Telescope (HST) legacy field with three JWST instruments and five coordinated parallel observing modes. The complete program involves imaging with the Near Infrared Camera (NIRCam; Rieke et al. 2003, 2005; Beichman et al. 2012; Rieke et al. 2022) short-wavelength (SW) and long-wavelength (LW) channels in 10 pointings, observed as coordinated parallels to primary observations with the Near Infrared Spectrograph (NIRSpec; Jakobsen et al. 2022) and the Mid-Infrared Instrument (MIRI; Rieke et al. 2015; Wright et al. 2015). Four of the 10 pointings will be additionally covered by NIRCam wide-field slitless spectroscopy (WFSS) with MIRI imaging obtained in parallel. The complex CEERS survey layout results in multiple sets of overlapping observations, allowing for cross-instrument comparisons and enabling explorations of galaxies from $\sim$1 to 20 μm. The EGS field is additionally covered by an extensive set of multiwavelength observations including imaging and spectroscopy with ground-based observatories, HST, and the Spitzer Space Telescope, from surveys including the Cosmic Assembly Near-infrared Deep Extragalactic Legacy Survey (CANDELS; Grogin et al. 2011; Koekemoer et al. 2011), the MOSFIRE Deep Evolution Field Survey (MOSDEF; Kriek et al. 2015), and the DEEP2 Galaxy Redshift Survey (Newman et al. 2013).

The CEERS survey is optimized for the study of galaxies in the early universe ($z > 10$) and the processes of galaxy assembly and black hole growth for redshifts in the range $z \sim$ 1–10. The NIRCam and MIRI imaging will provide number counts of $z > 10$ candidate galaxies, robust stellar mass estimates for galaxies at $z > 4$, probes of dust-obscured star formation and supermassive black hole accretion at $z \sim$ 1–3, and detailed measurements of source morphologies. Multi-object spectroscopy with NIRSpec's microshutter assembly (MSA) and NIRCam's WFSS will provide spectroscopic redshifts of sources at $z \sim$ 5–12 through rest-UV and/or rest-optical emission lines, helping to constrain models of chemical evolution in the interstellar medium. The full details of the CEERS science goals and observing strategy will be presented in S. Finkelstein et al. (2023, in preparation).

In this paper, we present the CEERS team reduction of our NIRCam imaging, providing a detailed description of our processing steps with the JWST Calibration Pipeline. Building on our team's extensive experience from HST's CANDELS program, we have developed a number of custom processing steps and modifications to the Calibration Pipeline that improve on aspects such as imaging noise, detector features, alignment, and global background modeling. Alongside this paper we will announce the first public release of our NIRCam images (CEERS Data Release 0.5 or DR0.5), available for download at ceers.github.io/releases.html and on MAST as High Level Science Products via doi:10.17909/z7p0-8481. We include in this release scripts for downloading the raw NIRCam imaging and processing it through the Calibration Pipeline along with all our custom scripts.

As part of our preparations for reducing the real NIRCam imaging, we created extensive simulations to replicate the CEERS observing strategy and expected detector noise and artifacts as closely as possible. These simulations help validate methods for source detection, photometry, and morphological measurements and were instrumental in building our strategies for working with the real NIRCam data. We have previously released our simulations as part of the CEERS Simulated Data Releases, which are available at the same website, and have also included NIRSpec MSA, NIRCam WFSS, and MIRI imaging simulations.

This paper is organized as follows. In Section 2, we describe the CEERS NIRCam observations obtained to date. We describe our image reduction in detail in Section 3, presented in three stages (Sections 3.1, 3.2, and 3.3). We discuss our custom corrections to remove snowballs (Section 3.1.1), wisps (Section 3.1.2), and $1/f$ noise (Section 3.1.3). In Section 3.3, we present the processing steps required to create combined mosaics, including astrometric alignment (Section 3.3.1), resampling (Section 3.3.2), and a custom background subtraction (Section 3.3.3). We discuss known issues present in our reduced data products in Section 4, and we briefly summarize in Section 5. We also provide detailed appendices, with a description of our released mosaic images (Appendix A), brief summaries of previous NIRCam data reduction versions that were used in early publications by the CEERS team (Appendix B), and a comprehensive discussion of the creation and reduction of our simulated NIRCam imaging (Appendices C and D). We express all magnitudes in the AB system (Oke & Gunn 1983) unless otherwise noted.

2. CEERS Epoch 1 Observations

Due to the observability of the EGS field and the need for self-overlap of the CEERS observing modes, CEERS is schedulable in June or December, with a 180° position angle rotation between these times achieving similar survey layouts. Due to time constraints in the 2022 June observing window following telescope and instrument commissioning (EGS observability ends on July 1), the CEERS observations were split into two epochs. The first epoch was executed on 2022 June 21. This involved CEERS pointings 1, 2, 3, and 6, which were observed with MIRI as the primary instrument and NIRCam in parallel. The remaining CEERS observations (six NIRSpec MSA+NIRCam imaging pointings and four NIRCam WFSS+MIRI imaging pointings) are scheduled for 2022 December. We note that the current MIRI and NIRCam observations do not overlap, but many of the MIRI pointings
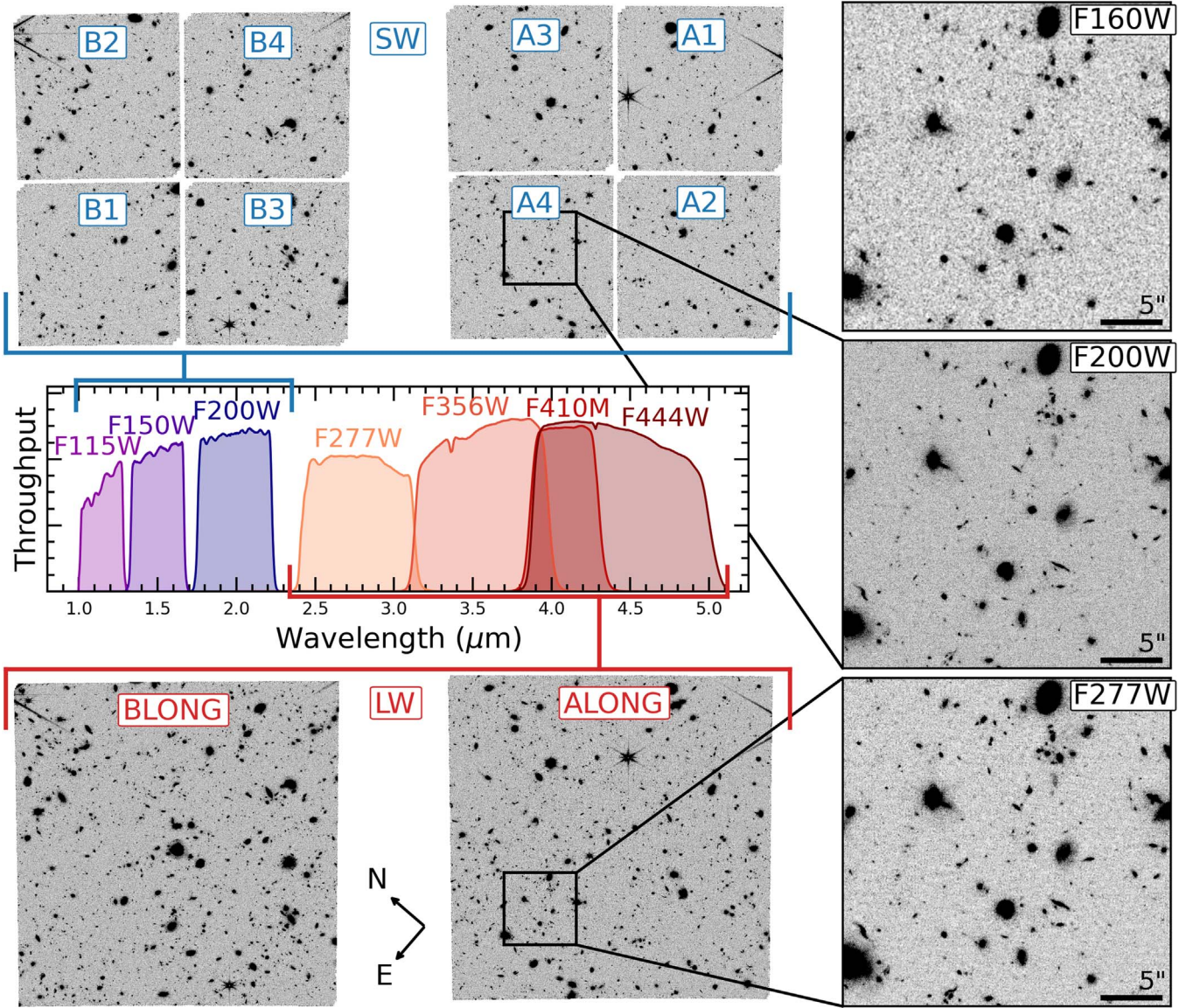
Figure 1. An illustration of the CEERS NIRCam observations, using NIRCam1 as an example. We show an SW (F200W) mosaic on the top left and an LW (F277W) mosaic on the bottom left. The SW and LW detectors are labeled in blue and red, respectively. The large module gap is visible in both mosaics, and the SW detector gaps are visible in the F200W mosaic. The CEERS filter throughput curves are plotted in the middle, with SW filters shown in purple-blue and LW filters in orange-red. Along the right edge, we show $29'' \times 29''$ zoom-ins of the mosaic, with the same portion of the HST F160W mosaic displayed on top for reference. The black bars in the lower right corners of the zoom-in panels indicate a $5''$ scale. We note that the orientation of this image is flipped $180°$ with respect to the orientation of the NIRCam field of view in documentation. The orientation of this figure matches that of the NIRCam mosaics released as part of CEERS DR0.5.

will have NIRCam coverage once the rest of the survey observations are completed in December. In this paper, we focus on the CEERS Epoch 1 NIRCam observations (hereafter referred to as NIRCam1, NIRCam2, NIRCam3, and NIRCam6) and reduction.

The NIRCam instrument (Rieke et al. 2003, 2005; Beichman et al. 2012) consists of two modules, A and B, each of which has a field of view covering $2'.2 \times 2'.2$. The modules are separated by a $\sim45''$ gap, making the total combined NIRCam field of view ~9.7 arcmin^2. Each module has four SW detectors, A1–A4 and B1–B4, tuned for observations in the range 0.6–2.3 μm, and one long-wavelength LW detector (ALONG and BLONG, 2.4–5 μm). Together, the SW detectors cover approximately the same area as the LW detectors, though they are separated by $\sim5''$, leaving gaps in the SW mosaics that are not present in the LW mosaics. Observations in the SW and

LW channels are obtained simultaneously. For CEERS Epoch 1, we have paired the following SW and LW filters together: F115W+F277W, F115W+F356W, F150W+F410M, and F200W+F444W. The filters are observed in this order to ensure that fading persistence from previous observations will not mimic a Lyman break in our images. In Figure 1, we show the seven NIRCam filters, as well as a SW (F200W) and LW (F277W) mosaic of NIRCam1, with each individual detector labeled. The primary MIRI imaging is obtained with seven filters (see Table 1): F560W, F770W, F1000W, F1280W, F1500W, F1800W, and F2100W. The CEERS MIRI imaging and reduction will be presented in G. Yang et al. (2023, in preparation).

We use a three-point dither pattern chosen to optimize the subpixel sampling and bad pixel mitigation for both NIRCam and primary MIRI observations. As MIRI dithers are required

Table 1
CEERS Epoch 1 NIRCam Observations

Filters		N Groups	Exptime
NIRCam	MIRI		(s)
NIRCam1 Field Center: 14:19:56.2+52:58:38.8			
F115W+F277W	F770W	5	1546.1
F115W+F277W	F1000W	5	1546.1
F115W+F356W	F1280W	5	1546.1
F115W+F356W	F1500W	5	1546.1
F150W+F410M	F1800W	5	1546.1
F150W+F410M	F2100W	5	1546.1
F200W+F444W	F2100W	9	2834.5
NIRCam2 Field Center: 14:19:34.8+52:54:50.3			
F115W+F277W	F770W	5	1546.1
F115W+F277W	F1000W	5	1546.1
F115W+F356W	F1280W	5	1546.1
F115W+F356W	F1500W	5	1546.1
F150W+F410M	F1800W	5	1546.1
F150W+F410M	F2100W	5	1546.1
F200W+F444W	F2100W	9	2834.5
F200W+F444W[a]	F2100W	9	2834.5
NIRCam3 Field Center: 14:19:12.7+52:51:03.5			
F115W+F277W	F560W	9	2834.5
F115W+F356W	F770W	9	2834.5
F150W+F410M	F770W	9	2834.5
F200W+F444W	F770W	9	2834.5
NIRCam6 Field Center: 14:19:25.2+52:49:56.0			
F115W+F277W	F560W	9	2834.5
F115W+F356W	F770W	9	2834.5
F150W+F410M	F770W	9	2834.5
F200W+F444W	F770W	9	2834.5

Note. All images are obtained in parallel with MIRI imaging as the primary instrument mode. All exposures use the MEDIUM8 readout pattern and a three-point dither pattern determined by the MIRI PSF. The exposure times listed are the total including dithers.

[a] This observation was repeated at a slightly different PA on 2022 June 28 owing to a problem with the MIRI observations, but it is heavily affected by persistence; see Section 3.1.4 for details.

to be $>3 \times$ the FWHM of the MIRI point-spread function (PSF), the dither steps are determined by the MIRI filter for each observation. Specifically, we use the dithers `3-POINT-MIRI-[filter]-WITH-NIRCam`, where `filter` is the primary MIRI filter. (The exception is for the observations with MIRI filter F560W, for which a custom dither pattern was not available, and so we adopt that for F770W.) As a result, different dither step sizes are sometimes used for images in the same NIRCam filter. However, as illustrated in Figure 1, most of the dithers are not large enough to cover the SW detector gaps. Our NIRCam exposures use the MEDIUM8 readout pattern with either five or nine groups and one integration. The total exposure time is ~3000 s in each filter, with double the exposure time in F115W for added depth in the Lyα dropout filter for $z \gtrsim 9.5$ galaxies. Exposure times for each observation are listed in Table 1.

Finally, due to an onboard problem with MIRI pointing 2 at the time of observation, the last set of MIRI+NIRCam exposures in this pointing was reobserved on 2022 June 28 (see footnote a in Table 1). The original NIRCam observations were not affected. As a result, there is a second set of F200W +F444W imaging in this field at a slightly different position angle, providing added depth in these two filters. We note,

however, that these additional images seem to be heavily affected by persistence (see Section 3.1.4 for a discussion). See Table 1 for details on Epoch 1 NIRCam observations and S. Finkelstein et al. (2023, in preparation) for more information on the CEERS Survey and observation specifications.

3. Image Reduction

We process the raw images through the JWST Calibration Pipeline created and maintained by STScI (hereafter jwst), with custom steps and modifications informed from our work with the simulations described in Appendix D. The reduction described here and used to create our first public data release uses jwst version 1.7.2 and Calibration Reference Data System pipeline mapping (CRDS[33] pmap) 0989, which includes in-flight NIRCam dark, distortion, bad pixel mask, read-noise, and superbias reference files. It also includes the ground flats corrected for in-flight performance released on 2022 August 18 (pmap 0951) and the updated photometric calibration reference files[34] released on 2022 October 4. Pipeline mapping 0989 corresponds to the NIRCam instrument mapping (imap) 0232.

In the following sections we describe our image reduction steps in detail. We will also provide the parameter files for each pipeline step, custom Python routines for the additional corrections we have applied, and batch scripts for running all steps on all four NIRCam pointings on GitHub.[35] These scripts are summarized in Table 2 for reference. We invite the reader to use these scripts and parameter files to reproduce our reduction.

3.1. Stage 1—Detector-level Corrections

Stage 1 of the JWST Calibration Pipeline performs detector-level corrections, many of which are common to all instruments and observing modes. The reduction steps involve initializing the data quality (DQ) arrays for flagging pixels, identifying saturated pixels, subtracting the superbias, using reference pixels to correct for readout noise, correcting pixels for nonlinearity, subtracting the dark current, identifying cosmic rays as jumps in each pixel's up-the-ramp signal, and calculating a linear fit to the unflagged ramp data to determine the average count rate per pixel. The end product of Stage 1 is a count-rate image in units of counts s^{-1}. We adopt the default parameter values for these steps. We run the reduction steps of Stage 1 together with the snowball correction described in Section 3.1.1, using the Python script `snowball_wrapper.py` described in the following section. For reference we also provide the pipeline parameter file `detector1_1.7.2.asdf` with the equivalent set of default parameter values.

In the following subsections, we describe some features of the NIRCam images for which we have developed custom corrections. We refer the reader to Rieke et al. (2022) and Rigby et al. (2022) for more information on detector performance and some of these features that were discovered and characterized during commissioning.

---

[33] jwst-crds.stsci.edu
[34] www.stsci.edu/contents/news/jwst/2022/an-improved-nircam-flux-calibration-is-now-available
[35] github.com/ceers/ceers-nircam

Table 2
CEERS NIRCam DR0.5 Reduction

Reduction Step	Script Name	Discussion in Text
Stage 1 + snowball correction	`snowball_wrapper.py`	Sections 3.1, 3.1.1
Wisp subtraction	`wispsub.py`	Section 3.1.2
$1/f$ noise removal	`remstriping.py`	Section 3.1.3
Stage 2	`image2_1.7.2.asdf`	Section 3.2
SkyMatch + outlier detection	`image3_part1.asdf`	Section 3.3
Astrometric alignment	`run_tweakreg.py`	Section 3.3.1
Individual background subtraction + variance map rescaling	`skywcsvar.py`	Section 3.3.2
Mosaic creation	`image3_nircam[pointing]_[chn].asdf`[a]	Section 3.3.2
Mosaic background subtraction	`mosaic_background.py`	Section 3.3.3

Note.
[a] We use different parameter files for creating SW and LW mosaics, where the only difference is the input-to-output pixel size ratio. Here `chn` refers to either the SW or LW channels.

3.1.1. Snowball Correction

"Snowballs" are large cosmic-ray events that can affect hundreds of pixels and have a circular morphology on the NIRCam detectors. We see an average of ∼25–30 snowballs per detector in a ∼900 s exposure. The fluence of counts in the center of the snowballs is very high and can sometimes saturate the detector. The cosmic-ray flagging step of jwst often successfully identifies and flags the central cores of these large cosmic rays, leaving the more diffuse wings of the snowballs present in the count-rate maps output by Stage 1. The top left panel of Figure 2 shows an example of a count-rate map containing multiple snowballs that were only partially removed by the pipeline.

We identify snowballs as large contiguous sets of pixels in the `GROUPDQ` arrays that have been flagged as jumps (`JUMP_DET`). We found it helpful to divide the snowballs into two tiers: large ones, which require a rather large mask to address the extended wings, and smaller ones, which do not require masking as much additional area. In order to separate snowballs from smaller cosmic-ray impacts, we median-filter the `GROUPDQ` arrays with separate two-dimensional top-hat kernels with radii of 7 and 15 pixels to identify the smaller and larger snowballs, respectively. This filtering recovers extended groups of pixels that have an approximately circular footprint. We also include in the snowball mask any saturated pixels that are within these big groups. We then grow the resulting snowball footprints via binary dilation and a two-stage top-hat growing kernel with radii of 7 and 35 pixels. We add this updated snowball mask to the `GROUPDQ` array and run the ramp-fitting step from jwst Stage 1. The flux in the affected pixels is determined by the remainder of the ramp, using the slope of the ramp excluding the newly identified cosmic-ray jump. The top middle panel of Figure 2 shows the DQ array for the count-rate map in the left panel, with the original footprints of the snowballs identified with red contours. The top right panel shows the output count-rate map that results from performing this snowball correction. In the bottom row, we show the portion of the mosaic that corresponds to the region displayed in the top row to demonstrate the effectiveness of this correction.

The snowball correction is performed with our Python script `snowball_wrapper.py`, which runs Stage 1 of the pipeline, saves the ramps from the first run of the ramp-fitting step, identifies the snowballs and grows their footprint, flags them as
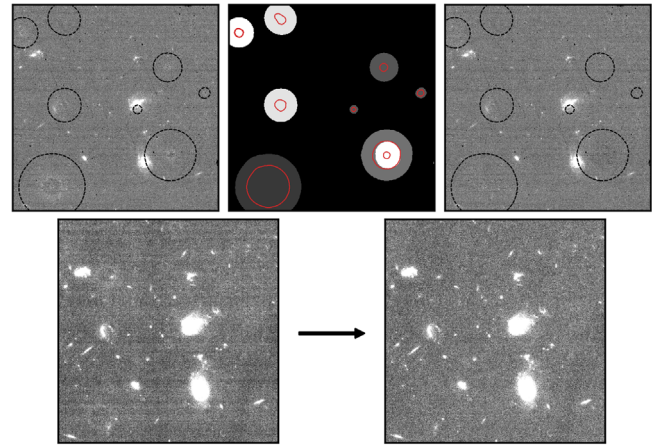

Figure 2. An example of the snowball correction. In the top row we show a portion of an F115W count-rate map that includes several snowballs. The left image shows the output of the default jwst, where there is a particularly large snowball present in the lower left corner of the image. The middle shows the mask generated by identifying and growing the snowball footprints, where the red contours identify the original footprints. The snowballs are color-coded by the group in which they were detected; brighter snowballs were detected in later groups. The right panel shows the count-rate map resulting from refitting the ramp with the updated snowball mask added to the `GROUPDQ` arrays. The dashed black circles show the new footprints of the snowballs and are there to guide the eye. In the bottom row we show the portion of the F115W mosaic that corresponds to this region. In the left panel, the mosaic has been created without correcting for the snowballs in the individual exposures, while the right panel shows a mosaic that included this correction. (Three input images contribute to this mosaic, and so there are some snowballs present in the bottom left panel that are not in the snowball mask in the top row because they come from one of the other two dithers.) The three CEERS dithers are not sufficient to compensate for the presence of snowballs. This additional correction is needed to remove them from the coadded mosaics. We note that the left panel also includes $1/f$ noise, which we discuss in Section 3.1.3.

cosmic rays, and then runs the ramp-fitting step again to create a count-rate map that excludes the flagged portions of the ramps.

We note that persistence from the saturated cores of very bright snowballs can show up in subsequent exposures. These are faint enough not to be rejected when the dithered images are combined. They can show up as single-band detections that look a lot like faint emission-line galaxies. For pure emission-line sources in WFSS exposures, it is important to inspect the individual exposures and their DQ arrays.
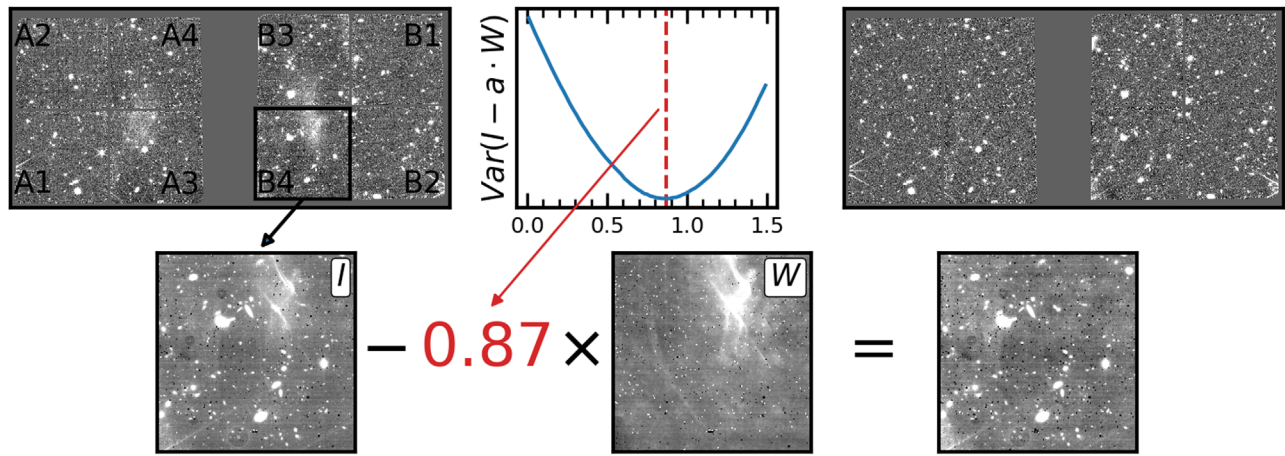
Figure 3. An illustration of our wisp subtraction process. The top left panel shows the full extent of the wisps in an F200W mosaic of CEERS NIRCam pointing 1. We then illustrate the process of fitting the wisp templates using one F200W image from detector B4 as an example. We minimize the variance of the wisp template W scaled by a factor a and subtracted from the image I in order to find the best-fitting a (0.87 in this case). The bottom right panel shows a cleaned version of the F200W image where the wisp feature has been removed. The top right panel shows the full F200W mosaic for this pointing once the wisps are subtracted from all affected input images. The three images in the bottom row have been smoothed by a Gaussian kernel with $\sigma = 2$ pixels for display purposes. We note that while we show a DR0.5 mosaic in the top row of this figure, the orientation of the mosaic has been rotated $180°$ to align with the NIRCam field of view. The images in the bottom row therefore display the wisp feature as it would appear on an individual B4 detector.

3.1.2. Wisp Subtraction

We next subtract the "wisp" features from the F150W and F200W images. Wisps are created from stray light reflected off the secondary mirror supports. They are visible on detectors A3, A4, B3, and B4 and are most prominent in F150W and F200W. The strength of the wisp features depends on the source of the reflected light, and so the wisps can have a variable brightness from exposure to exposure. The top left panel of Figure 3 shows a version of the F200W mosaic for CEERS NIRCam pointing 1 from which we have not subtracted the wisps as an example of the large-scale structure of this feature. They extend across two detectors in each module.

The NIRCam team has provided wisp templates constructed from images obtained by several NIRCam commissioning and ERS programs observed early in Cycle 1. At the time of this writing, two sets of templates have been released, in 2022 July and August. Both sets of templates are available on the JWST User Documentation page on Claws and Wisps.[36] We use the updated wisp templates released on 2022 August 26, which are the result of reprocessing the original observations with updated processing steps and reference files, including a correction for the large-scale variations in the ground flats consistent with that introduced by pmap 0956.

We scale the templates to account for the variable brightness of the wisp feature and subtract them from the images in the following way. We first apply the flat field to each image to match the flat-fielded templates and to measure the wisp feature in the flattened images. For each image, we perform a very "cold" source detection (i.e., a very high detection threshold of 5.5σ) with Photutils (Bradley et al. 2020) to identify and mask out large, bright sources in the image while avoiding the wisp feature itself. Next, we smooth the wisp template with a Gaussian kernel with $\sigma = 2$ pixels. For an array of coefficients a, we find the value that minimizes $\sigma^2_{\mathrm{MAD}}(I - aW)$, where

σ_{MAD} is the median absolute deviation, I is the flat-fielded masked image, and W is the smoothed wisp template. We find that in almost all cases we need to scale the wisp template by a factor <1. We scale the original (unsmoothed) wisp template by a and subtract it from the original (un-flat-fielded and unmasked) image. We illustrate this process in Figure 3.

While this scaling does well at removing the large-scale feature, our wisp subtraction is still preliminary. The current wisp templates were produced with an updated but still early NIRCam reduction. Additionally, in early Cycle 1 observations, the dithers were often small compared to the size of the sources observed. As a result, some ghost images of bright sources are present in some of the wisp templates and therefore become regions of oversubtraction (by $\sim$3%–4%) in the CEERS images. We also note that we see some evidence for the presence of weak wisps in F115W, but as there are no templates available for this filter, we leave it uncorrected. The wisp templates will be improved throughout Cycle 1 with additional observations and updates to the NIRCam reduction and reference files.

3.1.3. 1/f Noise Subtraction

Our final custom step on the count-rate images is to measure and remove $1/f$ noise, which is correlated noise introduced in the images when the detectors are read out (Schlawin et al. 2020). The noise presents as horizontal and vertical striping patterns that vary from row to row and column to column. Ideally, this noise would be fit and removed during the reference pixel fitting or the up-the-ramp fitting of jwst, an update that may be included in future versions of the Calibration Pipeline. In the meantime, we perform our own correction for $1/f$ noise in each individual count-rate map as follows.

As an additive effect, the noise pattern should be removed before applying the multiplicative flat-field correction, yet the striping patterns are best measured on flat images. We therefore apply the flat field to the count-rate maps for pattern measurement, but we subtract it from the original count-rate images. We next mask all bad pixels (with a DQ flag value >0)

---

[36] The updated templates are packaged in wisps_2022_08_26.tgz available at jwst-docs.stsci.edu/jwst-near-infrared-camera/nircam-features-and-caveats/nircam-claws-and-wisps.
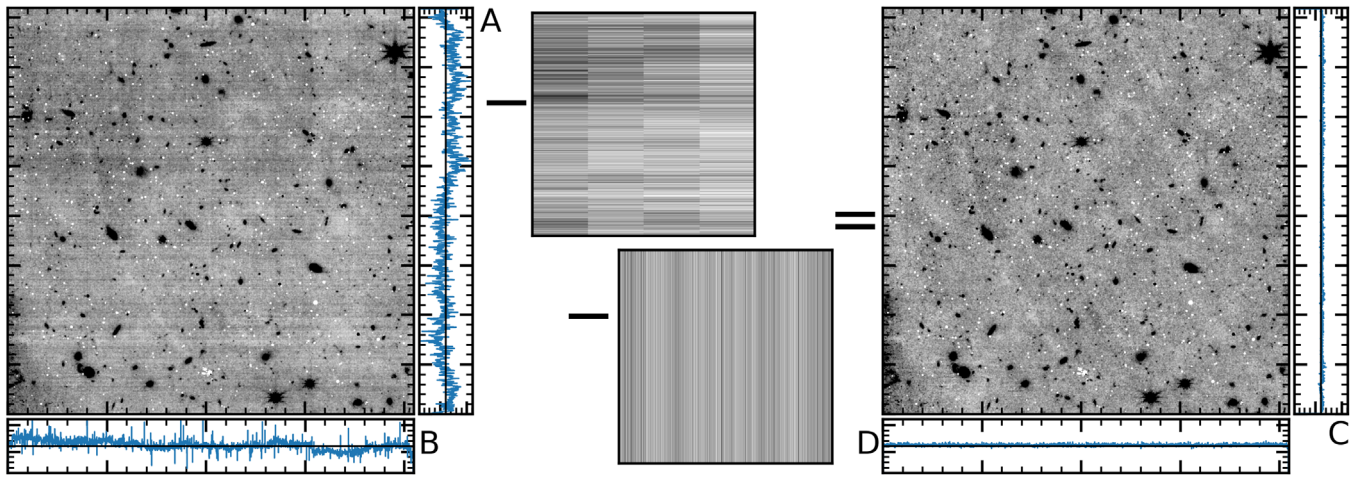
Figure 4. An illustration of our process for removing $1/f$ noise from count-rate maps. The image on the left shows an input count-rate map in F200W affected by $1/f$ noise. We show the median pixel value measured in the unmasked portions of each row (A) and column (B) in blue along the right and bottom edges, respectively, showing significant variation due to $1/f$ noise. The middle panels show the horizontal and vertical striping patterns that we identify using the unmasked portions of the image. The amplifier-dependent pattern is visible as the four vertical quadrants in the horizontal striping model. The image on the right shows the result of subtracting both models, where the right (C) and bottom (D) panels show that the noise in the image has been significantly reduced. All four panels displaying the median pixel values (A–D) are plotted with the same limits ±0. The count-rate maps are flat-fielded and smoothed by a Gaussian kernel with $\sigma = 2$ pixels.

and source flux that is identified with Photutils using a tiered source detection method. This method consists of convolving the image with progressively smaller kernels and running a segmentation-style source detection at each step. In this way we are able to detect both large, extended sources and small, compact sources with detection parameters optimized for each source size. We use four tiers, with Gaussian kernels of $\sigma = 25$, 15, 5, and 2 pixels (on the original $0\farcs031$ and $0\farcs063$ pixel^{-1} scales for the SW and LW channels, respectively). These values were chosen after experimenting with several filter kernels to aggressively mask as much source flux as possible. Next, we calculate a pedestal value for the sky background by fitting a Gaussian to the distribution of pixel values in the masked image.

We measure the striping pattern using a sigma-clipped (2σ) median along first rows and then columns. For the row correction (horizontal striping), we measure and remove the pattern individually for each of the four amplifiers. In some images, especially in the SW filters, the difference from amplifier to amplifier can vary by $\sim$3%–5%, and so this amplifier-dependent correction works better than using the median from the full row. However, in some cases, especially around bright or extended sources, a large number of pixels in a given amp-row are masked, leaving too few to calculate a robust median. In these cases, we use the median of the entire row for the affected amp-row. The threshold used to determine the cutoff in number of masked pixels per amp-row varies from image to image to allow for the best pattern subtraction. We illustrate this amp-row and column subtraction in Figure 4.

This amp-by-amp approach works well for NIRCam imaging, especially for fields like the EGS that are relatively sparsely populated (compared to a globular cluster, star field, or regions with high nebulosity, for example, where a majority of pixels in individual amplifier rows will be masked). However, it is not a good approach for NIRCam WFSS observations, where the length of a trace in the row grism is approximately the same size as an amplifier for some filters.

3.1.4. Additional Imaging in NIRCam2

The observations of CEERS MIRI pointing 2 on 2022 June 21 encountered a problem writing data to disk, and one of the F2100W (with NIRCam F200W+F444W in parallel) image sets was repeated on June 28. See G. Yang et al. (2023, in preparation) for a full discussion of the effect on the MIRI images. The NIRCam images from June 21 were not affected, and the repeated observations offer additional depth in F200W and F444W, though at a slightly different position angle. However, the repeat observations obtained on June 28 appear to suffer from significant persistence on SW detector A3.

We searched MAST for all NIRCam observations obtained in the 24 hr before the NIRCam2 repeat imaging. Program 1022 (PI: J Stansberry) observed Jupiter $\sim$6 hr before the CEERS imaging. This commissioning program aimed to test the Fine Guidance Sensor (FGS) guiding near a bright planet and to characterize the scattered light in each instrument. There were two observations obtained with Jupiter on SW detector A1 (F212N) and LW detector ALONG (F322W2). In both cases, the same illumination pattern is present on SW detector A3 as that we see in the CEERS images. We show the calibrated (processed through pipeline Stages 1 and 2, flat-fielded and in units of MJy sr^{-1}) A3 detector images from program 1022 in the top two panels of Figure 5. The pattern is fainter in the second image, obtained 20.3 minutes after the first, indicating that the pattern is fading with time as expected for persistence. The feature on the detector A3 images may be scattered light from Jupiter imaged off-detector, fading persistence that occurred while slewing, or fading persistence from an earlier observation. The program observed before 1022, and 8–10 hr before CEERS, is proprietary—GO 2473, PI: L Albert. Program 2473 targeted two brown dwarfs, WISE J053516.80–750024.9 and WISE J073444.02–715744.0, with NIRCam module B. The feature in the CEERS images is on the far side of the A3 detector from module B, and so we do not believe that the persistence was caused by observations from this program. We note that neither the observations of Jupiter on detector A1 nor any of the LW images left persistence in the CEERS images.
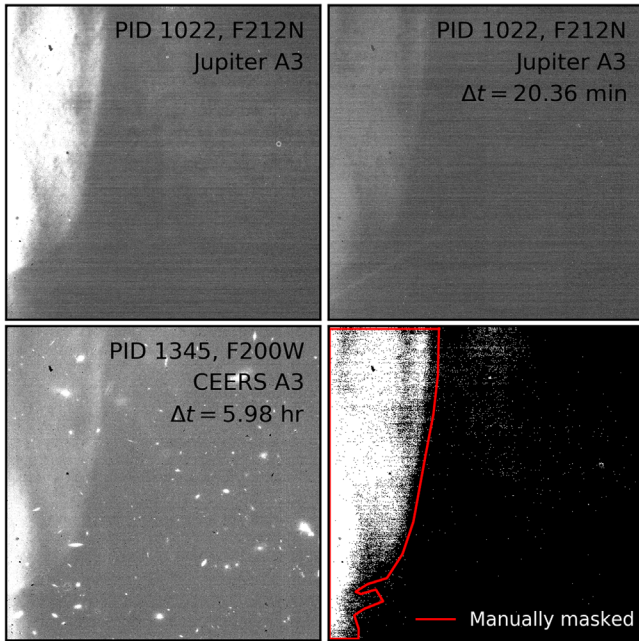
Figure 5. The persistence in the additional F200W imaging in NIRCam2. The top row shows persistent or scattered light present in A3 images of commissioning program 1022, in which Jupiter was observed on detector A1. These two images are displayed with the same zscale stretch to highlight how the illumination pattern is fading with time. One of the CEERS F200W exposures obtained ~6 hr later is displayed in the bottom left panel, where the same pattern is visible. We constructed a mask of pixels with elevated counts in both images from program 1022, shown in the bottom right panel. We then manually masked the pixels within the red histogram, necessary to mask the fainter edges of the pattern that otherwise are present in the final mosaic. None of the other detectors contain clear signatures of persistence. Regardless, a future reduction will include a more careful treatment of persistence in these observations.

We create a mask using the two A3 images from program 1022, identifying affected pixels as those with a flux >20 MJy sr^{-1} in the first exposure and >10 MJy sr^{-1} in the second exposure. These thresholds were found through trial and error to identify the persistent pattern and avoid flagging noise fluctuations. The bottom right panel of Figure 5 shows the mask we created in this way, with flagged pixels in white. However, we found that this mask was not sufficient around the scattered light pattern. The wings of the pattern were still present in our F200W mosaics, and so we manually masked out a region around the affected area, shown as the red polygon in Figure 5. This method represents a preliminary approach to handling the persistence in this field. In future data reductions, we will create a more careful mask incorporating the CEERS images to identify the fading pattern. Here we have also created a mask for detector A3 only. In the future we will explore persistence on all detectors.

We apply the mask to the snowball-corrected count-rate maps by setting the image pixels to zero in the science extensions and setting their DQ values to `DO_NOT_USE`. We then perform the corrections for wisps and $1/f$ noise as described above. We create three sets of mosaics in F200W and F444W for NIRCam2: one containing just the original imaging, one with just the repeated imaging, and one including both sets of imaging.

3.2. Stage 2—Individual Image Calibrations

Stage 2 of jwst involves steps such as flat-fielding the data and applying the flux calibration that converts the images from counts s^{-1} to MJy sr^{-1}. We adopt the default values for these pipeline steps. We note that the NIRCam flats used are ground

flats that have been corrected for an illumination gradient using in-flight observations. Additionally, the flux calibration is based on observations of three standard stars (PIDs 1536, 1537, and 1538) that have been observed across all 10 NIRCam detectors. It builds on the work of several teams, including the Resolved Stellar Populations ERS program (PID 1334; PI D. Weisz) observations of the globular cluster M92 (Boyer et al. 2022; Nardiello et al. 2022), zero-points derived by G. Brammer,[37] and early absolute flux zero-points from the NIRCam team (M. Rieke, private communication). Both the flat fields and the flux calibration tables are important reference files that will continue to be updated throughout Cycle 1.

3.3. Stage 3—Ensemble Processing

Stage 3 performs ensemble reduction steps, where the output product is a single mosaic per filter combining all images and dithers. These steps include astrometric alignment, background matching, outlier detection, and resampling the images onto a common output grid. We break this stage up into individual steps, first applying a customized astrometric correction and then running the `OutlierDetection` step of jwst Stage 3 with the default parameter values. Then, we background-subtract each individual file and perform two additional corrections on the variance arrays before resampling the images into one combined mosaic per filter. Finally, we perform a custom background subtraction of the mosaics to remove any residual background. In the following subsections, we describe these customized processing steps.

3.3.1. Astrometric Alignment

We perform an astrometric calibration using a modified version of the jwst TweakReg routine, with the modifications primarily aimed at exposing more fitting parameters and being able to input our own catalogs. We note that similar modifications have now been fully implemented in the official STScI pipeline. The TweakReg routine calculates the transformation needed to align images to an absolute WCS frame. It does this by comparing the source positions detected in each input image with their matches in a reference catalog. The early versions of TweakReg performed source detection largely internally, with few tunable parameters available to the user, and offered only a Gaia catalog as the absolute reference. With our modified version of this step, we create a SourceExtractor (Bertin & Arnouts 1996) catalog for each individual input image, providing improved source detection, deblending, and centroiding over the internal TweakReg source identification. We also use a custom reference catalog derived from an HST F160W 0″03 pixel^{-1} mosaic[38] in the EGS field with astrometry tied to Gaia-EDR3 (see Koekemoer et al. 2011, for further details on the methods for image processing and mosaic creation). In both cases we use the SourceExtractor windowed coordinates for improved centroiding, which especially improves positions for the compact sources that we primarily use for our alignment. We again note that these options are now available in the pipeline version of TweakReg, and so our modified version is no longer needed.

We calculate both a relative and absolute astrometric correction. The images are first aligned relative to each other, where shifts in x and y are determined between images of the same detector. This

[37] github.com/gbrammer/grizli/pull/107
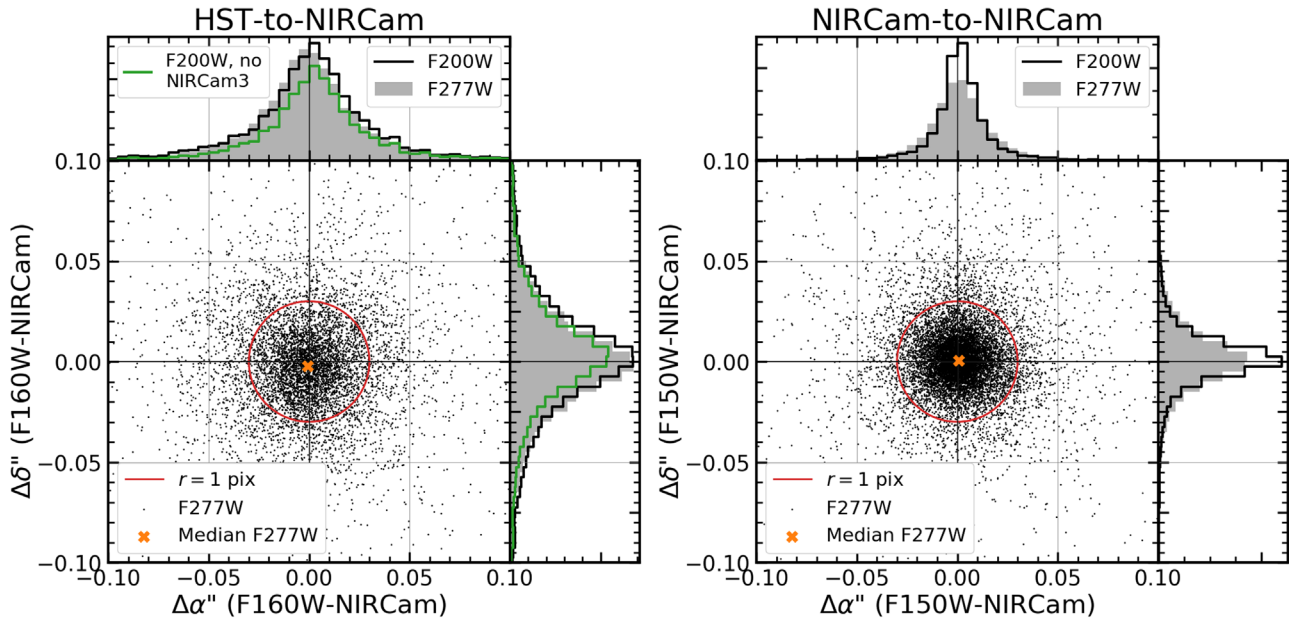[38] ceers.github.io/hdr1.html

Figure 6. Diagnostic plots of the CEERS NIRCam astrometric alignment. In the lefts panel we show the offsets for sources detected in all four pointings when compared with their positions in the HST F160W mosaic. The right panels show astrometric offsets compared with positions in the NIRCam F150W mosaic. The black points in the scatter plots show the offsets for source positions in the F277W images, and the orange cross indicates the median astrometric offset. The filled histograms show the distribution of offsets in R.A. and decl. for F277W source positions, and the open histogram shows the same for source positions in the F200W images. We show both an SW filter and an LW filter to indicate the quality of the astrometry in both channels. The red circles have a radius of 0″03, or 1 pixel in the output mosaics. Both cases show a median offset consistent with 0 and an rms scatter less than 1 pixel. The rms of the HST-to-NIRCam alignment is ∼12–15 mas, while that of the NIRCam-to-NIRCam alignment is ∼5–10 mas, generally smaller for the SW filters and larger for the LW filters. In the left panel, the green histogram indicates the F200W distribution excluding NIRCam3, the field that exhibits larger offsets relative to HST (see the text for details). The F277W distribution excluding NIRCam3 is very similar.

step accounts for uncertainties in the guide star alignment and pointing accuracy during dithering. The rms of this relative astrometry is ∼3–6 mas per source. The images are then aligned to the HST F160W reference catalog, allowing for *xy* shifts and rotations. In the LW images we also allow for a scaling factor to account for any additional distortion across the larger detectors, though we note that the calculated deviations from a unity scaling factor are small ($\sim 1 \times 10^{-5}$). The rms of this absolute alignment (WFC3-to-NIRCam) is ∼12–15 mas and is driven by the larger F160W PSF. The rms of the alignment between NIRCam images in different filters (NIRCam-to-NIRCam) is ∼5–10 mas, with SW images at the smaller end and LW images at the larger end of that range. Figure 6 illustrates the quality of the astrometry in F200W and F277W and shows both the HST-to-NIRCam and NIRCam-to-NIRCam alignments.

In summary, for all four NIRCam fields (1, 2, 3, and 6), for all filters and all detectors in both modules, the rms astrometric alignment quality is generally ∼5–10 mas per source between NIRCam filters (SW—LW) and ∼12–15 mas per source relative to the absolute frame defined by the HST F160W mosaic. There is, however, one exception to this: for NIRCam pointing 3, specifically for a ∼1′ region in the quadrant of the mosaic mostly covered by the B2 detector, the astrometric offsets relative to the HST F160W mosaic are larger, ∼0″05 (or about one-fifth of the 0″23 HST F160W mosaic PSF in this mosaic[39]). These offsets are also present in this region of the LW BLONG module, suggesting that it is not an alignment

problem with a specific SW detector. After detailed examination of the relevant data sets, a possibility is that the HST F160W exposures for the particular visit in that part of the mosaic were affected by a low-level guide star tracking issue, at the sub-PSF level (∼1/5 of a PSF), which can occasionally occur and is not always revealed by the guide star telemetry keywords in the image headers. Since these residuals are small compared to the size of the F160W PSF, they are unlikely to significantly affect the overall HST-NIRCam photometry since our apertures are generally substantially larger than the HST PSF. We therefore followed a different process for aligning this NIRCam pointing. We first aligned F277W to F160W, excluding all sources in the upper left quadrant of detector BLONG from the fit. We then used F277W rather than F160W as the reference catalog for all other filters in this pointing. The rms of the alignment is still ∼3–6 mas (relative) and ∼5–10 mas (absolute NIRCam-to-F277W).

3.3.2. Mosaic Creation

Before combining individual exposures into mosaics, we perform three additional corrections to the calibrated images. First, we subtract a pedestal value in MJy sr^{-1} from each exposure. This step is necessary because the SkyMatch routine of jwst does not successfully match the background across all detectors, likely because the small dithers result in little to no overlap between detectors. In order to calculate the background, we mask bad pixels and source flux using the tiered masks created for each image in Section 3.1.3. We then fit a Gaussian to the distribution of unmasked, sigma-clipped pixel fluxes and take the position of the peak as the image pedestal. This single value is subtracted from each image, and the headers are updated to reflect this value. Second, we

---

[39] Note that while the FWHM of the optical PSF of HST is 0″151 for F160W, this is subsequently convolved by (1) the WFC3/IR detector pixel size when the field is imaged, (2) a factor `pixfrac = 0.8` times the WFC3/IR detector pixel size, and (3) the mosaic pixel size, therefore yielding a final PSF FWHM of ∼0″23 in the F160W mosaic, which is standard for this instrument.

calculate the sky variance in each background-subtracted image. To do this, we mask sources in four tiers, as described in Section 3.3.3. We then block-sum the image in units of 7×7 pixels and use astropy's `biweight_midvariance` to make a robust estimate of the variance in blocks that have had no pixels masked. We estimate the equivalent per-pixel variance by dividing by the number of pixels per block (49). We then scale the read-noise variance array (`VAR_RNOISE`) to reproduce this value. Because `VAR_RNOISE` is used to compute the inverse variance that is used as weighting during the drizzle process, this ensures that the resulting error arrays do a good job of predicting the rms sky fluctuations (when estimated over large enough scales to avoid the pixel-to-pixel correlations introduced by drizzling).

Third, we make one final correction to the variance arrays to ensure that bad pixels are properly flagged. With our simulated mosaics (see Appendix D.4), we found that some known bad pixels had values of exactly zero in the variance arrays. When the dithered images were coadded, these areas in the output error array had relatively low rms compared with the average. In these areas, the input error array with the missing data or bad pixel did not contribute to the rms of the affected pixel. As a result, there were "holes" in the output error arrays in sets of three, matching our three dithers. Spurious source detections were more prevalent in these areas because the rms used for detection was low. For each individual image, we therefore replace any pixels that are exactly zero in the three variance arrays with values of infinity (`numpy.inf`). This correction ensures that the affected pixels are correctly down-weighted in the drizzling.

We create individual mosaics for each pointing using the Stage 3 routine `Resample`, which uses the drizzle algorithm with an inverse variance map weighting (Casertano et al. 2000; Fruchter & Hook 2002) to combine images into a single distortion-free image. The output mosaics are drizzled onto a common WCS with the same tangent point as the HST mosaics we have created in this field (see footnote 39). All HST and NIRCam mosaics are therefore pixel-aligned across all filters. The mosaics have pixel scales of $0\rlap{.}''03\,\mathrm{pixel}^{-1}$, and we chose not to shrink the input NIRCam pixels when drizzling (i.e., `pixfrac` = 1). This larger `pixfrac` is preferred for CEERS because the majority of the mosaic is covered by at most three exposures. The output pixel scale is only slightly smaller than the original scale in the SW channel ($0\rlap{.}''031\,\mathrm{pixel}^{-1}$) and just over two times smaller than that of the LW channel ($0\rlap{.}''063$). We discuss tests to evaluate the optimal drizzle parameters in Appendix D.4. The choice of `pixfrac` leads to increased pixel correlations in the output image, which we discuss in Section 4 and have not yet addressed in our mosaics.

These individual mosaics are included in our data release, and the files and extensions are described in Appendix A. We also created a set of combined, Epoch 1 mosaics that include all four pointings. Constructing these Epoch 1 mosaics requires considerable memory ($\sim$600 GB, depending on the filter), and so we use the Frontera computing system at the Texas Advanced Computing Center (TACC). Frontera provides a set of large memory nodes that offer 2.1 TB of memory each with the option to link multiple nodes.

3.3.3. Background Subtraction

Finally, we estimate and subtract any remaining background in the mosaics using a custom Python script that efficiently masks source flux before fitting the unmasked pixels with a two-dimensional model. The steps are outlined in Figure 7. The first step involves taking out large-scale fluctuations, masking bright pixels in the residual, and then running a large ring-median filter across that image to create the first good estimate of the background. The inner ring radius is $2\rlap{.}''4$, so this step preserves the wings of all but the largest galaxies in the image. This step creates background that is flat enough on large scales to permit us to mask sources above a fixed threshold without any perceptible gradients in source size and density due to large-scale changes in the background. We mask four tiers of sources, with tier number 1 intended to mask the most extended galaxies, moving progressively to the smallest galaxies at tier number 4. This is achieved by convolving the image with four different widths of Gaussians and masking areas with a minimum number N of connected pixels above a fixed threshold of 1.5σ. These masks are then grown by dilating them with a circular top-hat kernel with different kernel radii for each tier. We construct a source mask for each filter, including the pixel-aligned images in six available HST filters (F606W, F814W, F105W, F125W, F140W, and F160W). We merge all 13 separate masks into one, which is used to mask source flux in all filters. In this way we can exclude flux from sources that may be just below the detection threshold in some filters but not others.

We then measure the background in the unmasked regions using the Photutils `Background2D` class. We use the `biweight_location` estimator to robustly calculate the average background in sigma-clipped boxes of 10×10 pixels in a grid across the image. The resulting low-resolution gridded background model is then median-filtered over 5×5 adjacent boxes, and the `BkgZoomInterpolator` algorithm is used to interpolate the filtered array and construct a smooth background model.

A "before and after" example of background removal is shown in Figure 8. Any estimation of background requires decisions about what is "source" and what is "background." The procedure outlined above does a very good job of removing residual wisps and other artifacts in the NIRCam images, while preserving the wings of most of the galaxies of interest. However, it does suppress the wings of bright galaxies (intentionally) to enable the detection of faint neighbors.

To assess the background subtraction, we examined the stacked flux in pixels as a function of distance from the edge of the four separate tiers of masks. In most bands, for most tiers, there is very little "spillage" of galaxy flux into the pixels that were used to estimate the background. This spillage is impossible to avoid entirely. It is at a low enough level that we do not think the wings of galaxies that are above our detection threshold are significantly biasing the large-scale background estimation. In the left panel of Figure 9 we show an example for F200W in one of our fields.

On large scales, one would like to see the rms of the background approach the rms expected from a completely flat image affected only by the counting statistics of the incoming signal. The right panel of Figure 9 shows the per-pixel rms that is inferred from measuring the rms in source-free (i.e., unmasked) regions of an F200W image, when block-summed
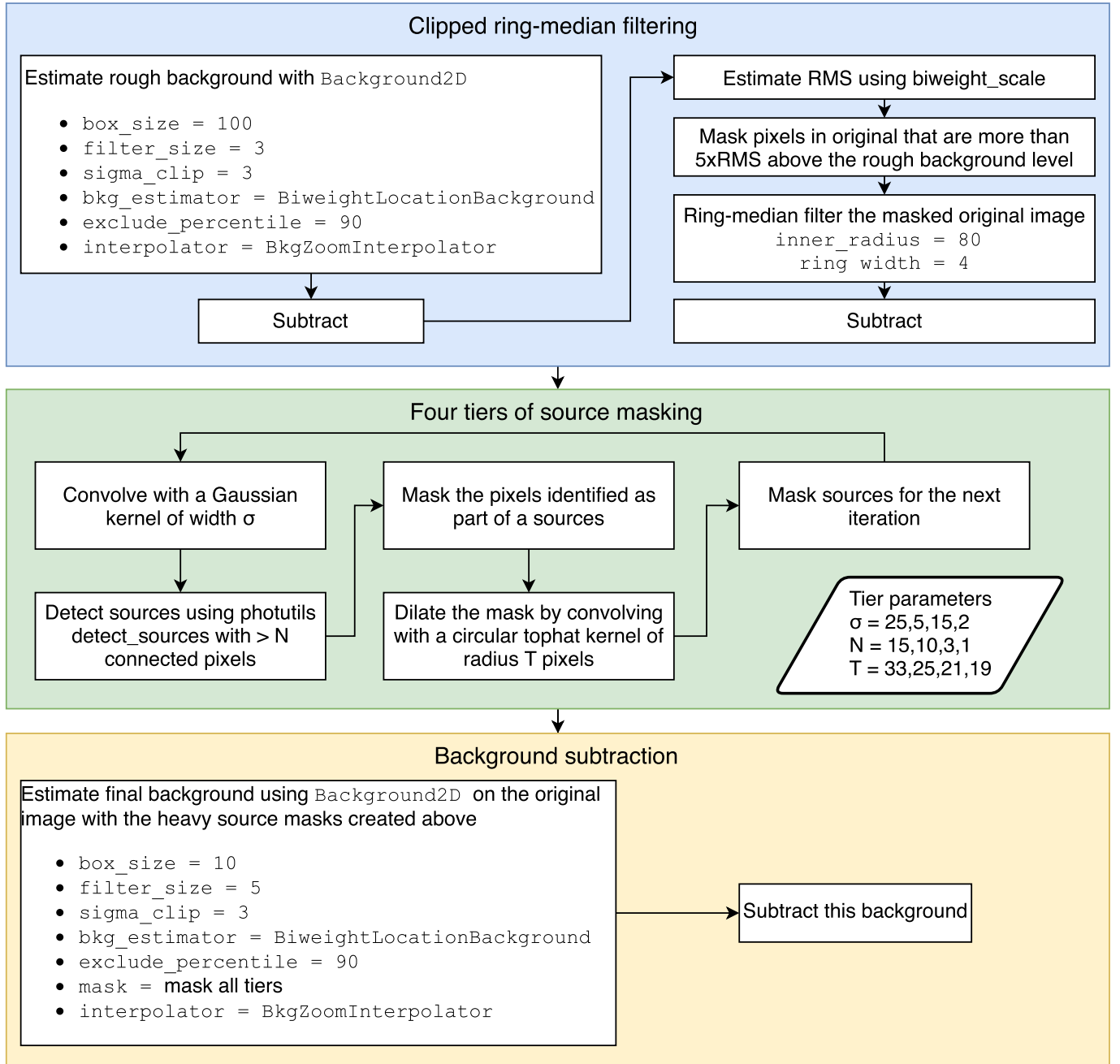
Figure 7. Steps for subtracting background from the coadded images.

over successively larger block sizes and then rescaled back to the per-pixel rms. On small scales, the rms is suppressed in the combined images because the drizzling procedure introduces a correlation between pixels. On medium scales, the residual wings of galaxies—which are impossible to remove entirely—slightly boost the rms. The rms approaches the ideal on larger scales, albeit with scatter in this measurement because there are very few blocks of 60×60 pixels and larger that are entirely source-free.

3.3.4. Field Depths

In Table 3, we present the 5σ limiting magnitudes in each filter and pointing. These depths are measured on our background-subtracted mosaics in circular apertures with radius $r = 0\rlap{.}''1$ and scaled to an empirical estimate of the noise in the image as described by Finkelstein et al. (2022b). Briefly, apertures ranging in size from $r = 0\rlap{.}''05$ to $r = 1\rlap{.}''5$ are placed across each image, avoiding source flux and bad pixels. A robust estimate of the 1σ noise is calculated in each aperture, and following the examples of Papovich et al. (2016), Bagley et al. (2022), and Finkelstein et al. (2022a; see also Labbé et al. 2003; Blanc et al. 2008; Whitaker et al. 2011), a second-order polynomial is fit to the noise as a function of aperture size. We use this function to estimate the noise in an $r = 0\rlap{.}''1$ aperture. Using stacked PSFs in each filter, we then measure the fraction of the total flux that is enclosed in an aperture of this size and
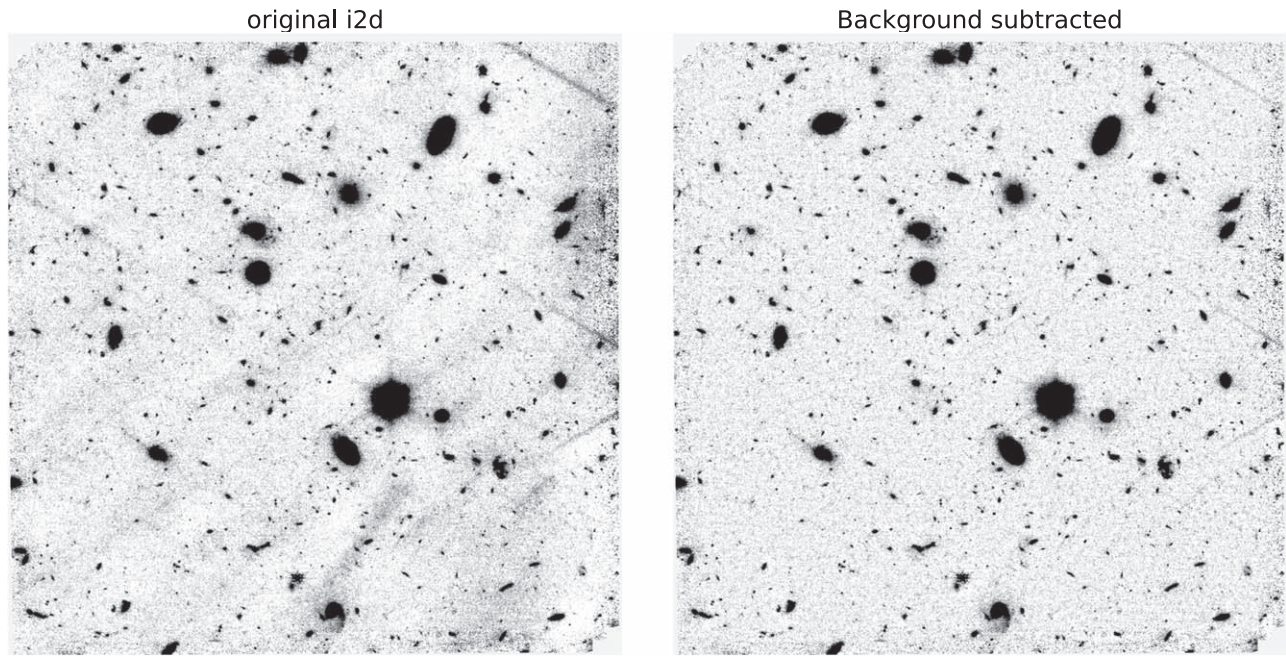
Figure 8. Example of background removal for a single detector in the F200W of CEERS field 1. The image on the left is the coadded image before background subtraction. The image on the right has had the fluctuating background removed as described in the text.

correct the noise estimate by this amount. See Finkelstein et al. (2022b) for a full description of each step in this process. The 5σ depths for each pointing and filter are listed in Table 3. For comparison, we also list estimates from v2.0 of the JWST Exposure Time Calculator (ETC), calculated for point sources in an aperture with radius $r = 0.''1$. The measured CEERS depths are consistent with the ETC estimates, ranging from ∼0.2% fainter to ∼0.3% brighter than the expectations. A color image of the Epoch 1 mosaic including all seven filters is displayed in Figure 10.

3.3.5. Flux Calibration

In this section, we explore the flux calibration of the CEERS mosaics, with the goal of identifying any residual corrections that may be needed to synchronize the zero-points in each detector. Ideally, this analysis would be performed by comparing the measured fluxes of the same set of sources when they are observed on different NIRCam detectors. However, due to the nature of the CEERS observing strategy, the NIRCam dithers are not large enough to observe a given source across multiple detectors, and so we do not have a direct test of detector-to-detector zero-points. We therefore explore the relative photometric calibration between detectors with two methods, which we describe below.

For the first method, we measured aperture photometry on NIRCam, HST/WFC3, and Spitzer/IRAC data for galaxies with $m < 24$ using Kron (1980) apertures. We used CANDELS HST mosaics (Grogin et al. 2011; Koekemoer et al. 2011) for the WFC3 filters and the Spitzer-Cosmic Assembly Deep Near-infrared Extragalactic Legacy Survey (S-CANDELS; PI G. Fazio) mosaics[40] (Ashby et al. 2015) for the IRAC imaging. As described by Ashby et al. (2015), the IRAC mosaics were created using Corrected Basic Calibrated Data exposures processed with IRAC Pipeline versions S18.7.0, S18.18.0,

and S19.1.0 and include the array position-dependent flux and pixel solid angle corrections. We first matched the NIRCam F115W PSF to that of WFC3 F125W, then used SourceExtractor in dual-image mode to measure source fluxes with identical apertures in the two filters, and finally compared these measurements detector by detector. We performed this analysis on the NIRCam mosaics, where each detector can be identified separately because the CEERS dithers are not sufficient to cover the detector gaps (see Figure 1). We repeated this same process comparing NIRCam F150W to WFC3 F160W, NIRCam F356W to IRAC 3.6 μm, and NIRCam F444W to IRAC 4.5 μm. We note that the passbands of these pairs of filters are not exactly the same, preventing us from using this method to obtain an absolute photometric calibration. Moreover, the derivation of absolute zero-points is challenging with extended sources owing to uncertainties in aperture corrections, making it difficult to separate the color-dependent correction for missing source wings from the flux calibration. Additionally, uncertainties in the PSFs used for image convolution and uncertainties in the local background determination in crowded regions contribute to making it challenging to use this comparison for an absolute calibration. Yet this approach of comparing NIRCam, WFC3, and IRAC fluxes in PSF-matched images (which we refer to below as "Method 1") should be robust for estimating relative calibrations between detectors provided that enough sources are used.

We use a second method for evaluating the relative flux calibration of the F200W, F277W, and F410M filters, for which there are no direct imaging data with comparable depth and spatial resolution available. For this "Method 2," we used the CANDELS photometric catalog (Stefanon et al. 2017) to obtain synthetic magnitudes in the NIRCam bands by convolving the filter transmission curves with the stellar population synthesis (SPS) models best fitting the spectral energy distributions of bright (F160W < 24 mag) galaxies. We then compared these synthetic magnitudes to Kron (1980) aperture photometry in the NIRCam images. As a test of the

---

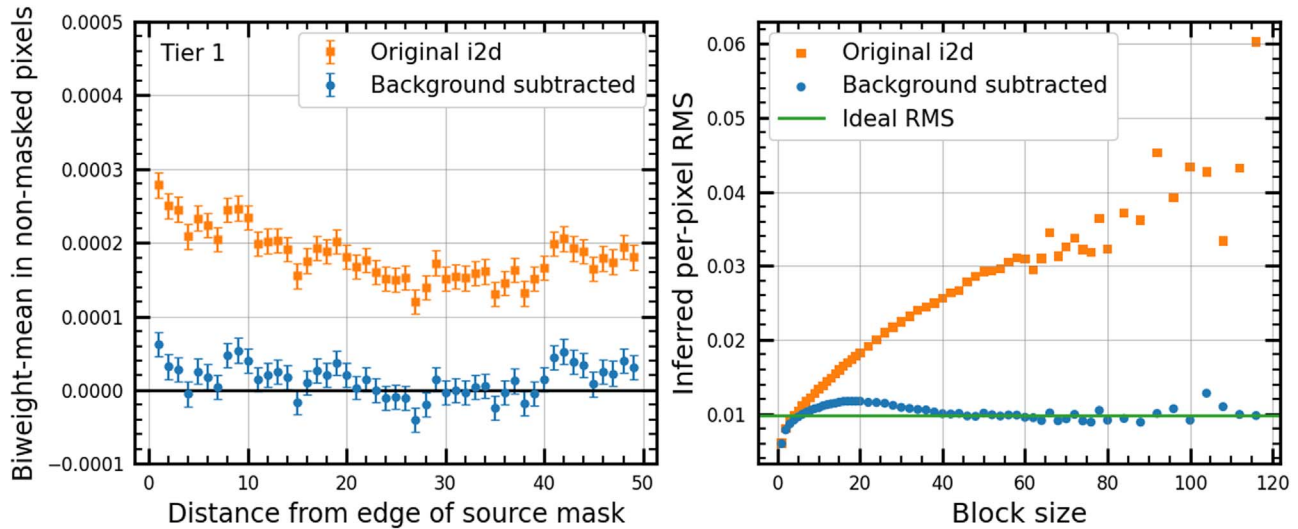[40] irsa.ipac.caltech.edu/data/SPITZER/S-CANDELS

Figure 9. Left: sky background around the borders of tier 1 of the source mask. Tier 1 has the largest convolution kernel and therefore masks the most extended sources. The diagram here shows the background (in MJy sr^{-1}) in unmasked pixels beyond the boundaries of the galaxies in this mask, as a function of distance to the closest masked pixel. One can see the overall elevated background level in the points from the original i2d file. There is a slight gradient toward brighter pixels closer to the boundaries of the masks, as expected from the faint extended wings of galaxies. The blue points show that the typical background is zero and that wings of the galaxies have been slightly suppressed. Right: statistics as a function of scale before and after background removal in the F200W image of NIRCam1. For each block size, the image has been block-summed in boxes of $N \times N$ pixels. The variance is then computed for blocks that had no pixels masked during the background estimation (i.e., these are our best effort at source-free regions of the image). The equivalent per-pixel rms from this estimate is $\sqrt{\mathrm{var}}/N$. The image coaddition suppresses the pixel-to-pixel rms on scales of a few pixels. On larger scales, the equivalent per-pixel rms continues to grow in the original image owing to the various nonuniformities. Some of these nonuniformities are from scattered light, but the procedure also suppresses the extended wings of bright galaxies. The fluctuations are suppressed on scales of more than about 40 pixels by the background subtraction procedure. The remaining fluctuations on intermediate scales are due to the wings of galaxies and to galaxies below the detection threshold. The green line shows the ideal rms expected if the sky fluctuations were due purely to photon counting statistics. This helps to confirm that the procedure has done an excellent job of removing large-scale nonuniformities in the image.

Table 3
NIRCam Pointing 5σ Depths

Filter	NIRCam1	NIRCam2	NIRCam3	NIRCam6	ETC
F115W	29.08	29.10	29.21	29.21	29.11
F150W	28.96	28.94	29.05	29.04	29.00
F200W	29.17	29.16	29.21	29.16	29.11
F277W	29.16	29.20	29.22	29.19	29.18
F356W	29.14	29.17	29.18	29.18	29.20
F410M	28.37	28.35	28.41	28.40	28.31
F444W	28.57	28.58	28.58	28.58	28.55
F606W	28.62	28.62	28.62	28.62	⋯
F814W	28.30	28.30	28.30	28.30	⋯
F105W	⋯	27.11	27.11	27.11	⋯
F125W	27.31	27.31	27.31	27.31	⋯
F140W	26.67	26.67	26.67	26.67	⋯
F160W	27.37	27.37	27.37	27.37	⋯

Note. Depths are measured for point sources in $r = 0\farcs1$ circular apertures and corrected to total flux using the flux measured for a stacked PSF within that aperture. The depths for NIRCam2 reported here are for the first set of observations only (obtained 2022 June 21) and do not include the additional imaging in F200W and F444W. The ETC estimates are based on exposures with five groups, matching the specifications of NIRCam3 and NIRCam6. We note that calculations with nine groups result in slightly lower depths in SW filters, matching what is measured for F115W and F444W in NIRCam1 and NIRCam2. All values are AB magnitudes. The depths in the HST filters are measured across the full EGS mosaics and so have the same reported values here for each individual NIRCam pointing. There is no WFC3 F105W coverage for NIRCam1.

performance of "Method 2," we used it to evaluate the NIRCam photometry in F115W, F125W, F356W, and F444W and compared the results to those obtained via "Method 1." For these four filters, we obtained consistent results with the two methods, compatible within 1%–2%, but with a 1.5× larger scatter for "Method 2." We conclude that "Method 2" provides a robust way to evaluate the relative flux calibration for F200W, F277W, and F410M.

Figure 11 shows our results comparing the detector-to-detector photometric calibrations for CEERS data reduced with CRDS pmap 0959 (red circles) and 0989 (blue circles). The pmap 0959 results are from an earlier reduction of the CEERS data, while the pmap 0989 results are those presented in this paper. In each case, we use "Method 1" with F115W, F150W, F356W, and F444W and "Method 2" with F200W, F277W, and F410M. We calculate the relative offsets of all SW detectors with respect to B1 and both LW detectors with respect to BLONG. We note that we have also compared our results for pmap 0959 (red circles) with those of Boyer et al. (2022), who used the globular cluster M92 to determine residual photometric offsets for this pmap. The relative detector-to-detector photometric offsets we measure using galaxies are consistent to within 1%–2% with those from Boyer et al. (2022) obtained with stars. Although stars are better suited for flux calibration, this comparison with Boyer et al. (2022) validates our approach for using galaxies to evaluate the flux calibration in CEERS imaging.

As can be seen in Figure 11, the improved flux calibration released with pmap 0989 (blue circles) reduces the detector-to-detector offsets that existed with the flux calibration of pmap 0959 (red circles). However, with pmap 0989, we still detect offsets between detectors at the <5% level, with a median of 2.5%. We do not apply these small offsets to our images at this time, but we warn the reader that the relative and absolute calibration of NIRCam images is still uncertain at the ~2%–4% level.
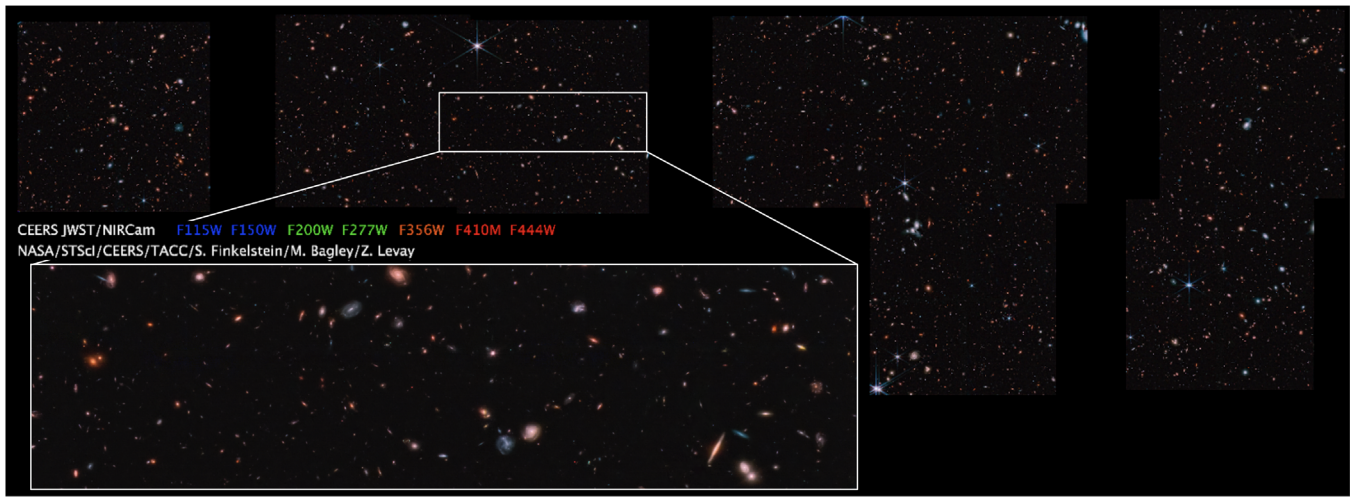
Figure 10. A seven-color image of the CEERS Epoch 1 NIRCam imaging. These images were reduced at TACC and colorized by Zoltan Levay. High-resolution versions of these images and related information are available at ceers.github.io/ceers-first-images-release.html.

Finkelstein et al. (2022b) have also explored the accuracy of the photometric calibration by exploring what average offsets in flux calibration would be needed to minimize the colors between observations and best-fitting spectral templates for a sample of several hundred spectroscopically confirmed galaxies. They also find that the calibration is good to 1%–2% in most bands, and no worse than ∼5% (in the bluest bands). Again, we note that these corrections were derived based on galaxies and thus depend on aperture corrections. Future photometric calibration updates based on stellar observations will reduce the amplitude of these corrections.

4. Known Issues

This first public data release of CEERS NIRCam imaging represents a best-effort reduction given the version of the jwst pipeline and calibration reference files available at the time. Several aspects of our reduction will be improved in future versions. We briefly summarize the known issues regarding this current version.

First, the set of calibration reference files (pmap 0989) still includes some that were created preflight (including the SW channel darks and the flats, which we discuss below). As discussed in Sections 3.2 and 3.3.5, the flats and flux calibration reference files are still preliminary. The current NIRCam flats are ground flats that have been corrected to account for illumination variations present in early observations. According to the CRDS database (see footnote 34), the large-scale variations in the flat fields have been corrected to ∼1%–2%, and ongoing programs to monitor sky flats and measure illumination patterns will continue to improve the flats. The photometric calibration reference files are the result of significant early efforts by the GTO and calibration teams, yet they are still based on only a handful of observations. In Section 3.3.5, the photometric residuals from detector to detector are at the ∼2%–5% level. The relative and absolute calibrations will continue to improve with more observations and monitoring of photometric standards observed on each of the 10 NIRCam detectors. These programs (e.g., PIDs 1536, 1537, 1538, and 1539, PI Gordon; 1475, 1476, PI Boyer) and others will deliver iterative improvements to the reference files throughout Cycle 1.

Second, as mentioned in Section 3.1.2, the templates used for wisp subtraction include some source ghosts. At the time of their creation, there were not enough observations with sufficient dithers to successfully remove all input sources from a combined stack. As a result, some small regions are oversubtracted (at the ∼3%–4% level) in the CEERS images when we subtract the scaled templates. The wisp templates will continue to improve as more programs obtain NIRCam imaging, allowing for cleaner stacks that capture the wisp patterns without contributions from sources. In the meantime, our background subtraction (Section 3.3.3) does an excellent job of removing any residual wisps or other background variations that may be introduced by our wisp subtraction.

Third, we note that the NIRCam3 and NIRCam6 mosaics exhibit more cosmic rays than the NIRCam1 and NIRCam2 images. This situation is expected given that the exposures in pointings 3 and 6 (a single dithered set of exposures per filter) are approximately two times longer than those in pointings 1 and 2 (where the depth is achieved in multiple sets of dithered exposures). In this reduction version, we have used the same reduction parameters for all four NIRCam pointings. In the future, we will tune the jump detection step of Stage 1 and the outlier detection step of Stage 3 to ensure that cosmic rays and outliers are appropriately identified and flagged in all exposures.

Fourth, we have not yet performed a careful check for persistence in the majority of the NIRCam images. We have masked out the very strong persistence in the additional F200W imaging in NIRCam2 (Section 3.1.4), and that correction itself was an initial attempt that can be improved. In a future version we plan to stack each dither in pixel space (i.e., not aligned in WCS space) and identify sources that do not move on the detector from exposure to exposure and also perhaps fade with time. However, this method will not be able to identify persistence affecting extended sources that are larger than the dither size. We expect this approach to work well in NIRCam1 and NIRCam2, which have a minimum of six exposures in most filters, but three exposures per filter should be sufficient to identify compact cases of persistence that can masquerade as high-redshift galaxies.

Fifth, in creating the resampled mosaics, we do not make any correction for correlated noise. As discussed in Section 3.3.2
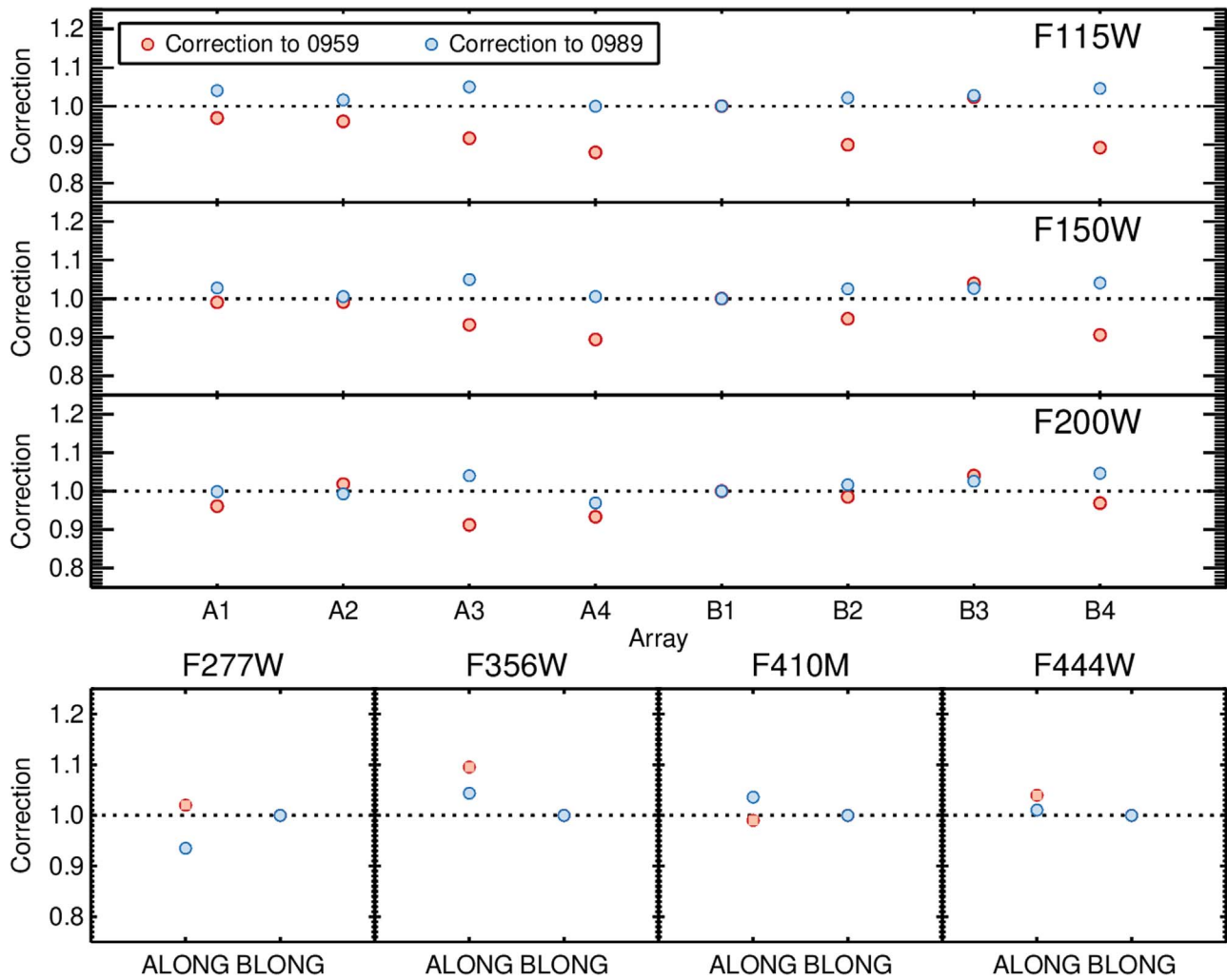
Figure 11. Evaluation of the relative detector-to-detector photometric calibration for the CEERS NIRCam data. We compare the photometry of sources in CEERS NIRCam imaging with that of HST/WFC3 and Spitzer/IRAC directly ("Method 1" described in the text) or with synthetic photometry ("Method 2") and normalize all offsets to the B1 and BLONG detectors. We performed this analysis for an earlier CEERS reduction using pmap 0959 (red circles). The measurements here can be interpreted as photometric offsets or corrections that should be applied to the flux calibration in pmap 0959. A reevaluation of the zero-point detector-to-detector offsets for the DR0.5 images released through this paper (calibrated with pmap 0989; blue circles) demonstrates the improvement in the flux calibration, while still indicating residual offsets at the 2%–4% level.

and Appendix D.4, we use `pixfrac = 1` so that each output pixel is sufficiently covered by input pixels in pointings where there are only three dithers. However, drizzling the full input pixels (i.e., without "shrinking" the pixels first) results in a mosaic with correlated pixels. In this case, the noise in the resampled science images and variance maps is reduced by the correlations, and so photometric uncertainties will by underestimated (e.g., Casertano et al. 2000; Labbé et al. 2003; Blanc et al. 2008; Whitaker et al. 2011; Papovich et al. 2016). We have rescaled the read-noise variance map to account for the sky variance (Section 3.3.2), but we have not yet applied any scaling to account for the pixel-to-pixel correlation introduced by the drizzling. This scaling can be estimated by computing the autocorrelation function of background, nonsource pixels and determining the amount to which the noise has been suppressed (e.g., Guo et al. 2013).

Finally, we note that the difference in depths between F115W and the other SW filters is less than expected compared with the prelaunch ETC. As the background at ~1 μm is low, the F115W images are dominated by read noise to a larger degree than expected during CEERS program planning.

Additionally, due to NIRCam's increased sensitivity compared with prelaunch predictions (Rieke et al. 2022; Rigby et al. 2022), the imaging in the other SW filters is slightly deeper than expected. As a result, the CEERS F115W images are comparable in depth to F150W and F200W, rather than the planned ~0.3 mag deeper. Updates to the reference files related to detector noise properties and to processing methods may improve the depth in F115W slightly. However, the measured depths are consistent with estimates from the in-flight ETC (v2.0; see Table 3), and so we expect that the CEERS F115W images will remain approximately the same depth as the other filters. This decrease in the dynamic range between F115W and F150W will limit the constraining power of photometric redshifts for sources close to the detection limit in F150W.

5. Summary

We announce the public release of CEERS NIRCam mosaics covering four pointings in the EGS field. These images were observed in 2022 June and obtained in parallel to primary MIRI imaging. The NIRCam imaging includes seven filters per

pointing (F115W, F150W, F200W, F277W, F356W, F410M, and F444W), reaching 5σ depths of $\sim$28.5–29.2 for point sources.

We have reduced the images using version 1.7.2 of the JWST Calibration Pipeline, with additional steps and modifications developed to handle challenges encountered with the data. In Section 3, we describe our image reduction process in detail, including our custom corrections for snowballs, wisps, $1/f$ noise, astrometric alignment, variance map scaling, and background subtraction. We produce mosaics in each filter and field, resampled onto a common output grid with a pixel scale of $0\rlap{.}''03$ pixel^{-1} and aligned with available HST imaging in the field. Our reduction scripts and pipeline parameter files are summarized in Table 2 and will be available and documented on GitHub. The images are the result of a best-effort reduction with the available jwst pipeline and calibration reference files early in Cycle 1. In Section 4, we summarize issues with the current reduction version that will improve with updated information about instrument performance.

Our publicly released mosaics are available at ceers.github. io/dr05.html and on MAST via doi:10.17909/z7p0-8481. In the appendices, we describe the file structure of the released images. We also describe previous CEERS NIRCam reductions that were used for results in some early CEERS publications.

Our reduction process has been heavily influenced by our work with our preflight NIRCam simulations. We describe the creation of these simulations in Appendix C, using as input a mock galaxy catalog constructed with the Santa Cruz semianalytic model (SAM), point sources, and real $z \sim 9$ candidate galaxies. We describe the simulated image reduction in Appendix D, including a test of drizzle parameters that informed our parameter choices with the real images. Our NIRCam simulations are available for download at ceers. github.io/sdr3.html.

Appendix A
Mosaic Image Structure

We have produced a multiextension fits file for each of the seven NIRCam filters for CEERS NIRCam pointings 1, 2, 3, and 6. These files are the result of all reduction steps described in Section 3. The files are available and documented at ceers. github.io/dr05.html and at MAST via doi:10.17909/z7p0-8481. The mosaics have 12 extensions, which we briefly summarize here:

1. SCI_BKSUB: resampled, background-subtracted science data, in units of MJy sr^{-1}
2. SCI: resampled science data (not background subtracted), in units of MJy sr^{-1}
3. ERR: resampled uncertainty estimates as standard deviation, constructed as the sum in quadrature of the resampled variance maps
4. CON: context image, which encodes information about the input images that contribute to each output pixel
5. WHT: weight image giving the relative weight of the output pixels, constructed from the VAR_RNOISE array during resampling
6. VAR_POISSON: resampled Poisson variance map
7. VAR_RNOISE: resampled read-noise variance map, which has been rescaled to include a robust estimate of the sky variance
8. VAR_FLAT: resampled flat-field variance
9. BKGD: the background model that was subtracted from the science image
10. BKGMASK: the tiered source mask used to create the background
11. HDRTAB: a table of FITS keyword values for all of the input images that were combined to produce the output image
12. ASDF: metadata for the JWST data model

The extension BKGD can be computed by subtracting the SCI_BKSUB extension from the SCI extension, but we include it in the mosaics for completeness.

We also provide images in six HST ACS and WFC3 filters, cut out from the full EGS mosaics and pixel-aligned to each

CEERS NIRCam pointing. While the background in the HST filters was already very close to zero, we have background-subtracted these mosaics for consistency with the NIRCam images and provide the HST mosaics both with and without this subtraction. The HST mosaics have five extensions, which we summarize here:

1. SCI_BKSUB: resampled, background-subtracted science data, in units of counts s^{-1}
2. SCI: resampled science data (not background subtracted), in units of counts s^{-1}
3. rms: resampled uncertainty estimates as standard deviation
4. BKGD: the background model that was subtracted from the science image
5. BKGMASK: the tiered source mask used to create the background

Appendix B
Earlier CEERS Data Reductions

Here we briefly describe the previous versions of the CEERS NIRCam data reduction that were used for results presented in early papers from the CEERS team.

B.1. Version 0.05, Zavala et al. (2023)

Zavala et al. (2023) presented results based on version 0.05 of the CEERS NIRCam reduction, which used jwst version 1.5.3 and pmap 0932 (NIRCam imap 0214). This reduction involved a preliminary correction for $1/f$ noise but did not correct for snowballs or wisps. The astrometric alignment for this version should also be considered preliminary. We calculated astrometric corrections for groups of images, rather than individually for each detector and dither. Specifically, we fit modules A and B separately for the LW images (grouping all dithers for a given filter and module together) and fit the SW images in three sets: (1) all module A detectors; (2) detector B2, which demonstrated significant offsets from the other B detectors; and (3) the remaining three detectors of module B. We first aligned the F200W images to the HST/WFC3 F160W reference catalog tied to Gaia-EDR3 and then used Photutils to create a new reference catalog in F200W. We cleaned the F200W reference catalog of all sources near detector edges and spurious sources around diffraction spikes and in the noise around bright sources and considered only compact sources in the magnitude range $18 < m_{200} < 27$. We aligned each NIRCam filter to F200w using the three groups mentioned above. The median astrometric offset in each filter and NIRCam pointing is $\lesssim 0\rlap{.}''005$, and the rms is $\sim 0\rlap{.}''025 - 0\rlap{.}''03$ (~ 1 pixel). However, for NIRCam pointing 2 in particular, the astrometry in the F115W and F150W filter suffered from a larger global offset of ~ 2–3 pixels. Additionally, the alignment between the images in each dither for this pointing was off by ~ 0.5 pixels, which slightly smeared out a small percentage of source flux, especially problematic for compact sources.

B.2. Version 0.07, Finkelstein et al. (2022b), Guo et al. (2023), and Kocevski et al. (2022)

Finkelstein et al. (2022b), Guo et al. (2023), and Kocevski et al. (2022) presented results based on version 0.07 of the CEERS NIRCam reduction, which used jwst version 1.6.2 and pmap 0942 (NIRCam imap 0221). This reduction version

included wisp subtraction and an improved $1/f$ noise removal. It did not include a correction for snowballs, though we note that the authors of each paper carefully inspected individual exposures to ensure that their results were not affected by snowballs. This reduction version also implemented the local background subtraction on the mosaics that is described in Section 3.3.3.

Finkelstein et al. (2022b) presented an earlier arXiv version that used version 0.05 (see previous section), where the improved astrometric alignment had a significant effect on their results. The measured F150W flux of the high-redshift candidate Maisie's Galaxy increased sufficiently in v0.07 to change the best-fit photometric redshift from $z \sim 14$ to a more tightly constrained $z \sim 12$. The authors have provided a full description of how the reduction version changed their results.[41]

Appendix C
Simulated CEERS NIRCam Imaging

In preparation for CEERS JWST/NIRCam imaging data, we created a series of simulated NIRCam images designed to reproduce the CEERS observing strategy. These simulations were designed to aid in our preparations with reducing the real imaging and to validate our photometry and analysis methods for the real NIRCam imaging. The simulations are performed with the Multi-Instrument Ramp Generator[42] (Mirage), with input sources taken from a mock catalog created using the Santa Cruz SAM for galaxy formation. In the following sections, we describe the simulation inputs and creation.

C.1. Santa Cruz SAM Mock Galaxy Catalog

The mock images are simulated based on an augmented version[43] of the mock galaxy catalog presented in Yung et al. (2022). The simulated light cone spans 782 arcmin^2, with coordinates overlapping with the observed EGS field and containing galaxies over redshift range $0 < z \lesssim 10$ and rest-frame M_{UV} range $-16 \gtrsim M_{UV} \gtrsim -22$. The galaxies in the mock light cone are simulated with the Santa Cruz SAM for galaxy formation (Somerville et al. 2015, 2021). Within dark matter halos extracted from the Bolshoi–Planck simulation (Klypin et al. 2016) and Monte Carlo merger trees generated with the extended Press–Schechter formalism (e.g., Somerville & Kolatt 1999), the SAM tracks the evolution of global galaxy properties under the influence of a set of carefully curated physical processes, including cosmological accretion, cooling, star formation, chemical enrichment, and stellar and active galactic nucleus (AGN) feedback. We refer the reader to Yung et al. (2022) for a schematic flowchart that illustrates the internal workflow of the SAM. The model configuration and physical parameters are based on the calibration from Yung et al. (2019a) and Yung et al. (2021). The models have been shown to reproduce the observed evolution in high-redshift (e.g., $z \gtrsim 4$) one-point distribution functions of M_{UV}, M_*, and star formation rate (Yung et al. 2019a, 2019b); observational constraints on the intergalactic medium (IGM) reionization history (Yung et al. 2020a, 2020b); and two-point autocorrelation functions from $0 \lesssim z \lesssim 7.5$ (Yung et al. 2022).

---

[41] web.corral.tacc.utexas.edu/ceersdata/papers/Maisie_update.pdf
[42] mirage-data-simulator.readthedocs.io
[43] https://ceers.github.io/sdr3.html#catalogs, SDR V3.

The full star formation and chemical enrichment histories of individual predicted galaxies are forward-modeled into rest- and observed-frame photometry with spectral energy distributions generated based on the SPS models of Bruzual & Charlot (2003). The observed-frame photometry is calculated accounting for dust attenuation effects using the attenuation curve of Calzetti et al. (2000) and for absorption by hydrogen along the line of sight in the IGM (Madau et al. 1996). In the CEERS mock catalogs, we also include self-consistently predicted nebular emission lines excited by young stars, AGNs, and post-AGB stellar populations in the high-resolution synthetic spectra and the broad- and medium-band photometry (Hirschmann et al. 2017, 2019; L.-Y. Yung et al. 2023, in preparation). Galaxies are added to the images as Sérsic profiles (Sérsic 1963, 1968), with Sérsic indices and effective radii determined as described in Brennan et al. (2015).

C.2. Additional Simulation Inputs

In addition to the mock galaxy catalog, we have added two additional sets of sources to the CEERS simulations. First, we have included the seven $z \sim 9$ galaxy candidates in the EGS field presented by Finkelstein et al. (2022a). This sample represents a significant (2σ) overdensity in the EGS field (Finkelstein et al. 2022a), including two spectroscopically confirmed galaxies at $z = 8.683$ (Zitrin et al. 2015) and $z = 8.665$ (Larson et al. 2022). The seven galaxies are added as Sèrsic profiles at their expected coordinates, and their JWST photometry is estimated using the best-fit EAZY template for each source's HST and Spitzer photometry.

Second, we included point sources in the NIRCam imaging simulations in two ways. The positions and magnitudes of bright ($V < 16$, Vega magnitudes) point sources in the EGS field are added from the Two Micron All Sky Survey, the Wide-field Infrared Survey Explorer, and Gaia. We added fainter point sources ($16 < V < 29$ Vega) using the Besançon Model[44] at mock positions to approximate the expected stellar density and luminosity distribution in the EGS field. In both cases, Mirage adds point sources from a library of PSFs, which was constructed using WebbPSF (Perrin et al. 2014). We use the default PSF library included with the Mirage reference files. This gridded library includes an image of the PSF core and an additional image of the PSF wings for each filter and pupil combination at a grid of positions across each detector. For each source, the appropriate PSF is selected from this library, the core is combined with the image of the wings, and the full PSF is normalized and scaled to the required brightness. The separation of the core and wings allows the user to tune the size of the PSFs in the simulated images. In the interest of decreasing processing time for the CEERS simulations, we adopted the default size of the PSF wing images (301×301 pixels) at all magnitudes. As a result, we note that the PSFs of some sources in our simulated images appear truncated. We found this to be an acceptable compromise, as our science goals for the simulations were focused on the identification and recovery of galaxy colors at high redshift.

C.3. Simulating Raw Images with Mirage

With these inputs, we use Mirage to construct raw NIRCam exposures that approximate the CEERS observations and include realistic estimates of noise, sky background level, and detector artifacts. The Astronomer's Proposal Tool (APT) file defines the observation specifications, setting the filters, readout modes and patterns, and dithers. At the time of our simulation creation, Mirage could not parse an observing setup with either MIRI or NIRSpec as the primary instrument and NIRCam imaging in parallel. However, as the parallel dithers are specified according to the primary observation (determined by either the size of the MIRI PSF or the NIRSpec nodding pattern), the combined primary+NIRCam parallel specifications were crucial. We therefore created a separate, NIRCam-only APT file with the same targets, the same number of dithers, and the same exposure specifications as the real CEERS program. We then replaced the pointing information of this NIRCam-only mock program with that from the original CEERS APT file. In this way, we were able to create a set of parameter files as input to Mirage that replicated all of the CEERS dither patterns. We note that this approach is no longer required, as Mirage can parse all observation templates and primary-parallel combinations.

The full CEERS NIRCam imaging simulation involves creating 1816 separate images, one image per exposure for each of the 10 NIRCam detectors. This total includes 75 exposures obtained in parallel to NIRSpec MSA observations, 57 exposures in parallel to MIRI imaging, and 56 exposures taken with the NIRCam WFSS observing mode. For these simulations we include just the imaging portion of the NIRCam WFSS observations, which amounts to a total of 24 direct image exposures in F356W and 56 SW exposures in F115W. We separately produced simulated CEERS NIRCam WFSS observations, which are available for download at ceers.github.io/sdr3.html.

For each simulated image, Mirage works in three stages. It first creates a noiseless seed image of the input point sources and galaxies, as well as any requested background signals. We adopted the beginning of the CEERS June observing window (2022 June 15–17) as simulated observing date, and Mirage used the jwst_backgrounds[45] tool to estimate the appropriate value for the EGS field on this date. In the second stage, Mirage reconstructs a dark exposure to match the required readout pattern with the specified number of groups and integrations. The use of ground-tested dark exposures introduces real detector effects such as the bias, known hot pixels, and detector noise properties. Finally, Mirage combines the dark with the seed image and adds additional effects such as cosmic rays. We used Mirage version 2.2.1 and the CRDS pmap 0834 (NIRCam instrument map 0193) for the input reference files.

Appendix D
Reducing Raw Simulated Data

While we leave the bulk of our discussion of our data reduction to Section 3, here we summarize our steps processing the raw simulated data. We do this for two reasons: (1) these processing steps informed our methods for working with the real CEERS NIRCam imaging, and (2) we aim to provide a

---

[44] doi:10.25666/osu-theta.20210107.galaxy-model

[45] github.com/spacetelescope/jwst_backgrounds

reference for how the simulated products were processed for any who wish to use them for science.

We process the raw simulated images through the three stages of the jwst pipeline, with custom scripts we developed to handle differences between the JWST reference files available at the time of simulation and the input assumptions of Mirage. The reduction uses jwst version 1.4.6, except where noted, and CRDS pmap 0834 for consistency with the simulated inputs. We adopt most of the default parameters for the jwst steps and describe any changes below. For the detector-level corrections applied in Stage 1, we apply the correction for interpixel capacitance, skipped by default, because Mirage adds this effect to the simulated data. We also supply custom gain maps for the steps that identify jumps in the up-the-ramp signal and fit the ramp to obtain a count-rate map. These custom gain maps were created to match the average value per detector that Mirage uses in creating the images, rather than the location-varying gain maps that were present in the reference files at the time.

Our first custom step is to remove the $1/f$ noise that is present in the images as horizontal and vertical striping. In short, this correction involves masking out all bad pixels and source flux (using the seed images for source positions and footprints) and collapsing each image along columns and rows to measure the striping pattern. We developed this correction in working with these simulated data and improved on the process for the real images. We describe this step in detail in Section 3.1.3.

D.1. Custom Flat Fields

Following the calibration steps of Stage 2, we perform a correction to remove residual large-scale but low-level features present in some of the images. The features correspond to areas on the detectors where the epoxy layer is thinner than for the unaffected pixels.[46] We found that these epoxy voids are multiplicative features in our simulated images and can be removed in a similar fashion to applying a flat field. The affected detectors are SW A1, A3, A4, B1, B3, and B4. In a previous version of our simulations (created using Mirage version 2.1.0, jwst version 1.3.3, and pmap 0764), we found a prominent feature only on detector A5 that is not present in our new CEERS simulations. We believe that the changing nature of these epoxy voids in our simulations may be caused by updates in the reference files used to add detector features to the images, such that the presence and strength of the features are determined by a combination of CRDS context and Mirage and jwst versions.

We therefore created custom flat fields for the six affected SW detectors in the following way. For each detector and filter we created 33 blank simulated images (chosen because each affected filter has at least 33 exposures across the full CEERS field) with no input sources and no cosmic rays added. We used the same input parameter files as used for the simulated images to ensure that the exact observation specifications were replicated. However, we changed the Poisson seeds so that the noise added to the blank images was pulled from a unique distribution. We processed the blank images following the same jwst and custom steps as the images containing sources.
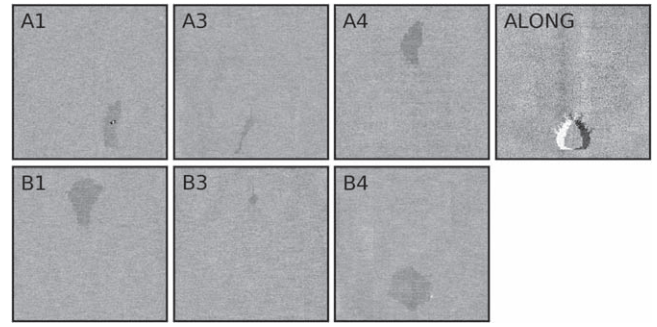
---

[46] See, e.g., STScI Technical Document, https://www.stsci.edu/files/live/sites/www/files/home/jwst/documentation/technical-documents/_documents/JWST-STScI-004622.pdfJWST-STScI-004622; Hilbert & Rest (2014).

Figure 12. Custom flat-field images we created for the reduction of our simulated images. We show the SW detectors A1, A3, A4, B1, B3, and B4, each of which has a different low-level feature present, caused by areas on the detectors with thinner epoxy layers. We use these six custom flats in reducing our simulated images. We also show an earlier custom flat we created for the LW detector ALONG. This feature was present in our SDR1 images and is included here for reference. With updated Mirage, jwst, and CRDS reference file versions, we no longer see this ALONG feature in our simulated images.

For the $1/f$ noise removal, we masked out the features so they would not contribute to the measurement of the striping patterns. After flat-fielding the blank images, we normalized each image by its median and combined all 33 using a weighted mean. The weights were taken as $w_i = 1/\mathrm{ERR}_i^2$, the uncertainty of the output flat field was estimated as $\sqrt{1/\sum w_i}$, and both the combined data and error arrays were normalized by the output image median. Figure 12 shows the six custom flats we created for the SW detectors. We also show a custom flat for LW detector ALONG that we created for a previous version of our simulated images (SDR1). This ALONG feature is not present in our current simulations and is included here for reference. We apply these six custom flats to the relevant detector images after the real flat is applied but before the flux calibration step that converts the images to MJy sr^{-1}.

D.2. Sky Subtraction

The final stage of jwst includes a step (SkyMatch) that computes sky values in a collection of images in a way that matches the sky levels of several images before they are combined to form a mosaic. However, we found that the SkyMatch step does not properly remove the background in simulated CEERS images when run on a collection of images. This is likely due to a mismatch between the input photometric calibration parameters used by Mirage in simulating the data and those used by jwst. Specifically, Mirage translates input magnitudes into count rates using HST-style PHOTFLAM values derived from filter throughput curves. Mirage uses the same PHOTFLAM value for all SW detectors for a given module and filter. The pipeline, however, converts count rates to MJy sr^{-1} using the PHOTMJYSR parameter in the flux calibration reference file, which depends on the pixel area and a mean gain value, both of which vary from detector to detector. A single value does not exist that can bring all simulated detector images to the same background level. Additionally, the CEERS dithers are not large enough to cover the gaps between detectors, and so there are many exposures with no overlap area in common for globally matching the sky values.

We find that the background levels in the final mosaics are significantly improved if SkyMatch is run on each calibrated image individually before mosaic creation. For this step, we adopt some minor changes to the default parameter values used

to calculate the sky statistics. We tested a grid of these parameter values and find that the following parameters yield output images with median backgrounds closest to zero for the CEERS simulated data. We set the upper and lower sigma clipping limits to 2σ (from the default of 4σ), the upper limit of usable pixel values for sky computation to 1 MJy sr^{-1}, and the number of clipping iterations to 10 (default = 5).

D.3. Astrometry and Outlier Rejection

Before creating mosaics, Stage 3 of jwst includes processing steps to apply astrometric corrections and identify outliers in the images. In real data, astrometric alignment is needed to account for uncertainties in guide star positions and to correct any remaining distortions or offsets between images from different detectors. However, as the simulated images are not created with astrometric errors or offsets from exposure to exposure, there is no need to perform this correction.

Next, the `OutlierDetection` step of jwst Stage 3 builds a stack of input images resampled onto a common grid in order to identify bad pixels or cosmic rays that were not detected in the `Jump` step of Stage 1. We found that a bug in the jwst version 1.4.6 pipeline sometimes calculated incorrect WCS bounding boxes for the stacks. Occasionally, the bounding box would exclude a portion of some input images, resulting in all source flux from the region being flagged as outliers. Therefore, we use jwst version 1.5.2 for the `OutlierDetection` step. Once outlier pixels are identified and flagged, we return to using version 1.4.6 for mosaicking for consistency with the rest of the reduction.

D.4. Simulated Mosaic Creation

Images are coadded in the Stage 3 step `Resample` as described in Section 3.3.2, with an output pixel scale of $0\rlap{.}''03$ pixel^{-1} and `pixfrac = 1`. We chose these drizzle parameters based on tests that we describe in the next paragraph, performed with simulated images of point sources. The mosaics are all drizzled onto a common WCS such that they are pixel-aligned across all filters, though they are not aligned with the HST mosaics, as the mock NIRCam sources do not have counterparts in the HST images. We note that, due to pixels with a value of exactly zero in the variance arrays of input images, there are "holes" present in the error arrays of our simulated mosaics as described in Section 3.3.2.

In order to determine the optimal output pixel scale and `pixfrac`, we created a simulated NIRCam pointing containing point sources and tested the FWHM recovery for different output pixel scales and `pixfrac` values. We placed 72 point sources across the image, with a magnitude $m = 23$ in all filters to avoid saturating the detectors in a CEERS-length exposure. This PSF simulation uses the observation specification of a NIRCam imaging pointing obtained in parallel to the NIRSpec MSA primary observations and so uses three small dithers determined by the NIRSpec nods. We explored output pixel scales of $0\rlap{.}''015$ and $0\rlap{.}''02$ pixel^{-1} in the SW images and $0\rlap{.}''03$ and $0\rlap{.}''04$ pixel^{-1} in the LW images. These choices are motivated by the need for the pixel scales of the SW and LW images to be integer multiples of each other (and all NIRCam images to be integer multiples of the available HST imaging) to maintain alignment. We tested `pixfrac` values ranging from 0.5 to 1.

In Figure 13, we show a summary of the results of these tests for F277W as an example (comparing mosaics with $0\rlap{.}''03$ and $0\rlap{.}''04$ pixel^{-1}). First, we measured the recovered FWHM of all 72 point sources. In the top left panel, we show the median recovered FWHM as a function of `pixfrac` normalized by the reported FWHM for this filter[47] ($0\rlap{.}''091$). The median of the recovered FWHMs increases toward larger `pixfrac` values, which is expected owing to the increased pixel-to-pixel correlations in the drizzled images. The recovered FWHMs are $\sim 5\%$ larger for the $0\rlap{.}''04$ pixel^{-1} scale, indicating a preference for the smaller pixel scale. We also calculated the standard deviation of the recovered FWHMs and plot these values normalized by the median recovered FWHM in the top right panel. For both pixel scales, the normalized σ_{FWHM} decreases with increasing `pixfrac`, an expected trend, as the output pixels more fully sample the PSFs.

Next, we measured the noise properties in the drizzled mosaics. In the bottom left panel of Figure 13, we plot the standard deviation of the sigma-clipped pixel values in the `VAR_RNOISE` maps normalized by the mean. These curves fall with increasing `pixfrac`, indicating that the width of the noise distribution decreases as more of each input pixel is incorporated into the output pixels. We also measured the fraction of pixels in the inverse variance maps ($1/$`VAR_R`$-$`NOISE`) that are a certain distance away from the median. In this way, we can quantify the number and magnitude of outlier pixels as a function of `pixfrac`. These curves are shown in the bottom right panel of Figure 13, color-coded by `pixfrac`. We once again see that the fraction of outliers decreases with increasing `pixfrac`. In the center of Figure 13, we show a small region of the `VAR_RNOISE` maps for each output pixel scale and `pixfrac`. These postage stamps are all displayed with the same scale and stretch and provide a visual representation of how well the output pixels are sampled in each mosaic. The read noise is reduced in mosaics with the larger pixel scale and/or larger `pixfrac`.

These tests informed our decision to create mosaics on output pixel scales of $0\rlap{.}''03$ pixel^{-1} and `pixfrac = 1`. This choice of `pixfrac` does result in maximum correlated noise introduced during the drizzle process, which we discuss in Section 4. We note that a `pixfrac` of 0.9 or 0.8 may also be acceptable, and we will explore these options more completely in a future reduction. We plan to use these mosaics (for both the simulated and real NIRCam data) for source detection and photometry in all filters. For future data releases, we will create SW mosaics on an output scale of $0\rlap{.}''015$ pixel^{-1} for use in characterizing source morphologies.

Finally, we note that the mosaic creation for the full CEERS simulated mosaic (all 10 NIRCam pointings) requires a considerable amount of memory. This version of the pipeline holds all images, variance maps, and weight maps in memory while resampling each onto the common output grid. With 928 input images, the F115W mosaic is especially memory intensive, requiring almost 1 TB of memory to resample all input images onto a $0\rlap{.}''03$ pixel^{-1} output image (and an estimated 3.5 TB for an output $0\rlap{.}''015$ pixel^{-1} scale). We therefore use the Frontera computing system at TACC to create these mosaics.

---

[47] The documented FWHMs are based on oversampled simulated PSFs created with WebbPSF. The PSFs will be updated during Cycle 1 based on in-flight measurements. See jwst-docs.stsci.edu/jwst-near-infrared-camera/nircam-performance/nircam-point-spread-function.
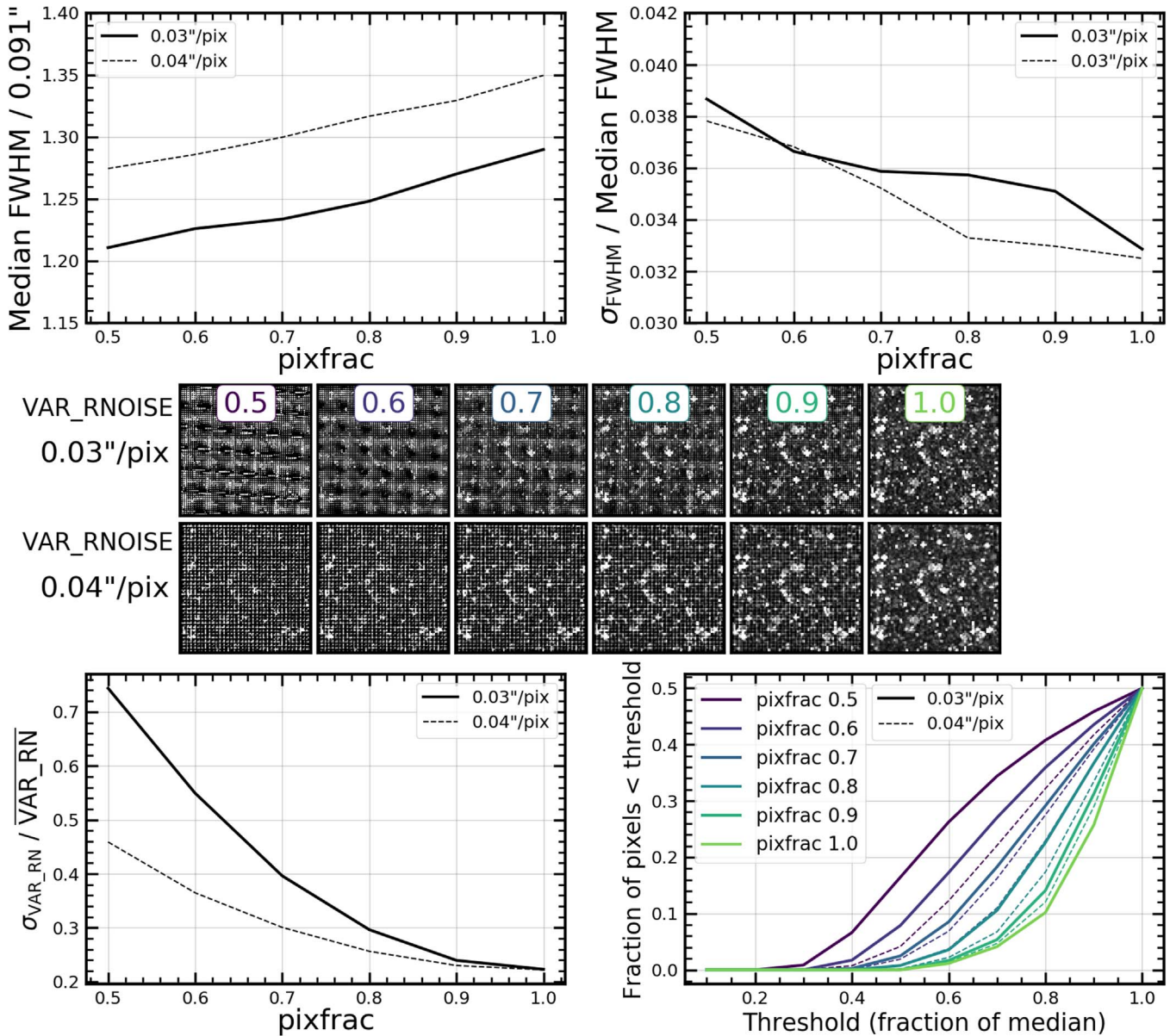
Figure 13. Example of the drizzle tests we performed with simulated images containing 72 point sources and varying the output pixel scales and `pixfrac` values. The plots here show results for F277W, for which we explored $0\overset{''}{.}03$ and $0\overset{''}{.}04$ pixel^{-1} output pixel scales. In the top row we show the median recovered FWHM normalized by intrinsic FWHM (left) and the standard deviation of the 72 recovered FWHMs normalized by the median (right), both as a function of `pixfrac`. In the middle panels, we show small regions of the `VAR_RNOISE` arrays for each pixel scale and `pixfrac`, all plotted with the same image stretch and scale. These panels illustrate the decreasing read noise with increasing pixel scale and/or `pixfrac`. In the bottom left panel we show the normalized standard deviation of sigma-clipped pixel values in the `VAR_RNOISE` as a function of `pixfrac`. In the bottom right panel we plot the fraction of pixels in the inverse `VAR_RNOISE` arrays that lie below various thresholds as a way to quantify the number of outlier pixels in each mosaic. These tests informed our choice to adopt an output pixel scale of $0\overset{''}{.}03$ pixel^{-1} and a `pixfrac` of 1 for the mosaics in our first data release.

D.5. Simulated Raw and Reduced Data Products

We have provided two sets of simulated NIRCam images as part of public CEERS data releases. In CEERS Simulated Data Release 1 (SDR1[48]), we shared a preliminary set of simulations of a single CEERS NIRCam pointing (labeled CEERS5), along with detailed step-by-step instructions for reducing the images in a Jupyter notebook. We also presented this work as part of JWebbinar 13. The mosaics released in SDR1 had pixel scales of $0\overset{''}{.}015$ pixel^{-1} in the SW filters and $0\overset{''}{.}03$ pixel^{-1} in the LW filters. Next, we shared an updated simulation and reduction of

this single NIRCam pointing in CEERS Simulated Data Release 3 (SDR3[49]). This follow-up release incorporated improvements in our input mock galaxy catalog and Mirage, as well as updates to jwst and the reference files available at the time. These mosaics were all drizzled to an output pixel scale of $0\overset{''}{.}03$ pixel^{-1} and were pixel-aligned across all filters. In Figure 14, we show the full CEERS simulated mosaic, including a panel zooming in to pointing 5, the pointing shared in SDR1 and SDR3. We further zoom in on simulated imaging in all filters of one of the real $z \sim 9$ candidates.

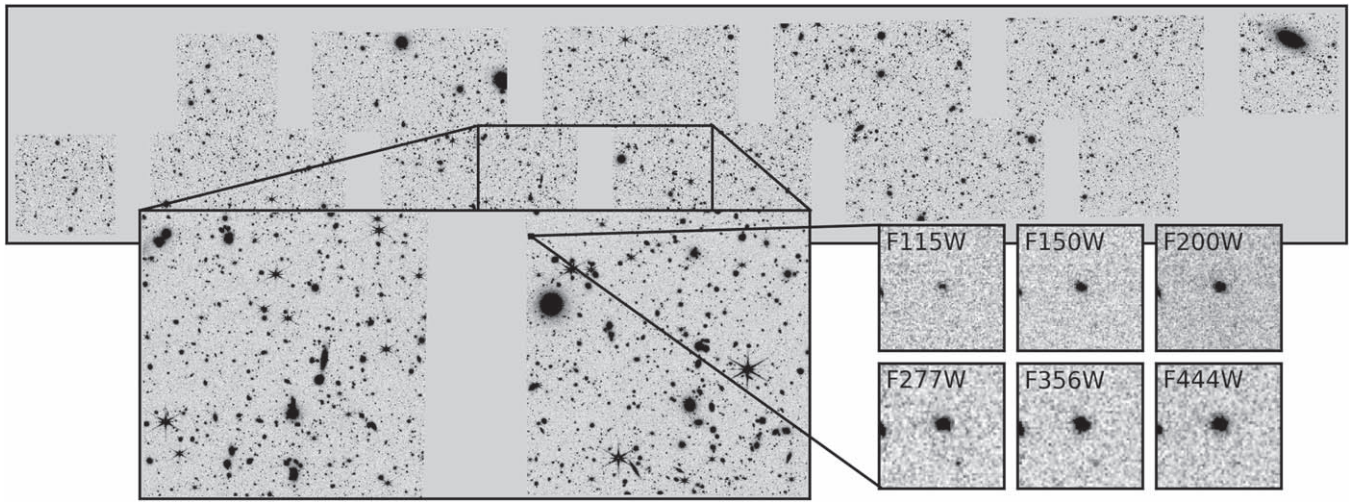[48] ceers.github.io/sdr1.html

[49] ceers.github.io/sdr3.html

Figure 14. The full CEERS simulated field, including all 10 NIRCam pointings. Here we show the F277W mosaic and a zoom-in around pointing 5, which was the focus of our early simulated data release. We further zoom in around one of the real $z \sim 9$ candidate galaxies that has been added to this field (see Section C.2). We show $3''$ postage stamps of the simulated images of this galaxy in all filters.

ORCID iDs

Micaela B. Bagley ● https://orcid.org/0000-0002-9921-9218
Steven L. Finkelstein ● https://orcid.org/0000-0001-8519-1130
Anton M. Koekemoer ● https://orcid.org/0000-0002-6610-2048
Henry C. Ferguson ● https://orcid.org/0000-0001-7113-2738
Pablo Arrabal Haro ● https://orcid.org/0000-0002-7959-8783
Mark Dickinson ● https://orcid.org/0000-0001-5414-5131
Jeyhan S. Kartaltepe ● https://orcid.org/0000-0001-9187-3605
Casey Papovich ● https://orcid.org/0000-0001-7503-8482
Pablo G. Pérez-González ● https://orcid.org/0000-0003-4528-5639
Nor Pirzkal ● https://orcid.org/0000-0003-3382-5941
Rachel S. Somerville ● https://orcid.org/0000-0002-6748-6821
Christopher N. A. Willmer ● https://orcid.org/0000-0001-9262-9997
Guang Yang ● https://orcid.org/0000-0001-8835-7722
L. Y. Aaron Yung ● https://orcid.org/0000-0003-3466-035X
Adriano Fontana ● https://orcid.org/0000-0003-3820-2823
Andrea Grazian ● https://orcid.org/0000-0002-5688-0663
Norman A. Grogin ● https://orcid.org/0000-0001-9440-8872
Michaela Hirschmann ● https://orcid.org/0000-0002-3301-3321
Lisa J. Kewley ● https://orcid.org/0000-0001-8152-3943
Allison Kirkpatrick ● https://orcid.org/0000-0002-1306-1545
Dale D. Kocevski ● https://orcid.org/0000-0002-8360-3880
Jennifer M. Lotz ● https://orcid.org/0000-0003-3130-5643
Aubrey Medrano ● https://orcid.org/0000-0002-8450-9992
Alexa M. Morales ● https://orcid.org/0000-0003-4965-0402
Laura Pentericci ● https://orcid.org/0000-0001-8940-6768
Swara Ravindranath ● https://orcid.org/0000-0002-5269-6527
Jonathan R. Trump ● https://orcid.org/0000-0002-1410-0470
Stephen M. Wilkins ● https://orcid.org/0000-0003-3903-6935
Antonello Calabrò ● https://orcid.org/0000-0003-2536-1614
M. C. Cooper ● https://orcid.org/0000-0003-1371-6019
Luca Costantin ● https://orcid.org/0000-0001-6820-0015

Alexander de la Vega ● https://orcid.org/0000-0002-6219-5558
Bryan Hilbert ● https://orcid.org/0000-0002-6875-1543
Taylor A. Hutchison ● https://orcid.org/0000-0001-6251-4988
Rebecca L. Larson ● https://orcid.org/0000-0003-2366-8858
Ray A. Lucas ● https://orcid.org/0000-0003-1581-7825
Elizabeth J. McGrath ● https://orcid.org/0000-0001-8688-2443
Russell Ryan ● https://orcid.org/0000-0003-0894-1588
Xin Wang ● https://orcid.org/0000-0002-9373-3865
Stijn Wuyts ● https://orcid.org/0000-0003-3735-1931

References

Ashby, M. L. N., Willner, S. P., Fazio, G. G., et al. 2015, ApJS, 218, 33
Astropy Collaboration, Robitaille, T. P., Tollerud, E. J., et al. 2013, A&A, 558, A33
Bagley, M. B., Finkelstein, S. L., Rojas-Ruiz, S., et al. 2022, arXiv:2205.12980
Beichman, C. A., Rieke, M., Eisenstein, D., et al. 2012, Proc. SPIE, 8442, 84422N
Bertin, E., & Arnouts, S. 1996, A&AS, 117, 393
Blanc, G. A., Lira, P., Barrientos, L. F., et al. 2008, ApJ, 681, 1099
Boyer, M. L., Anderson, J., Gennaro, M., et al. 2022, RNAAS, 6, 191
Bradley, L., Sipőcz, B., Robitaille, T., et al. 2020, astropy/photutils: v1.0.0, Zenodo, doi:10.5281/zenodo.4044744
Brammer, G. B., van Dokkum, P. G., & Coppi, P. 2008, ApJ, 686, 1503
Brennan, R., Pandya, V., Somerville, R. S., et al. 2015, MNRAS, 451, 2933
Bruzual, G., & Charlot, S. 2003, MNRAS, 344, 1000
Calzetti, D., Armus, L., Bohlin, R. C., et al. 2000, ApJ, 533, 682
Casertano, S., de Mello, D., Dickinson, M., et al. 2000, AJ, 120, 2747
Finkelstein, S. L., Bagley, M., Song, M., et al. 2022a, ApJ, 928, 52
Finkelstein, S. L., Bagley, M. B., Arrabal Haro, P., et al. 2022b, ApJL, 940, L55
Fruchter, A. S., & Hook, R. N. 2002, PASP, 114, 144
Gardner, J. P., Mather, J. C., Clampin, M., et al. 2006, SSRv, 123, 485
Grogin, N. A., Kocevski, D. D., Faber, S. M., et al. 2011, ApJS, 197, 35
Guo, Y., Ferguson, H. C., Giavalisco, M., et al. 2013, ApJS, 207, 24
Guo, Y., Jogee, S., Finkelstein, S. L., et al. 2023, ApJL, 945, L10
Hirschmann, M., Charlot, S., Feltre, A., et al. 2017, MNRAS, 472, 2468
Hirschmann, M., Charlot, S., Feltre, A., et al. 2019, MNRAS, 487, 333
Jakobsen, P., Ferruit, P., Alves de Oliveira, C., et al. 2022, A&A, 661, A80
Klypin, A., Yepes, G., Gottlöber, S., Prada, F., & Heß, S. 2016, MNRAS, 457, 4340
Kocevski, D. D., Barro, G., McGrath, E. J., et al. 2022, arXiv:2208.14480

Koekemoer, A. M., Faber, S. M., Ferguson, H. C., et al. 2011, ApJS, 197, 36
Kriek, M., Shapley, A. E., Reddy, N. A., et al. 2015, ApJS, 218, 15
Kron, R. G. 1980, ApJS, 43, 305
Labbé, I., Franx, M., Rudnick, G., et al. 2003, AJ, 125, 1107
Larson, R. L., Finkelstein, S. L., Hutchison, T. A., et al. 2022, ApJ, 930, 104
Madau, P., Ferguson, H. C., Dickinson, M. E., et al. 1996, MNRAS, 283, 1388
Nardiello, D., Bedin, L. R., Burgasser, A., et al. 2022, MNRAS, 517, 484
Newman, J. A., Cooper, M. C., Davis, M., et al. 2013, ApJS, 208, 5
Oke, J. B., & Gunn, J. E. 1983, ApJ, 266, 713
Papovich, C., Shipley, H. V., Mehrtens, N., et al. 2016, ApJS, 224, 28
Perrin, M. D., Sivaramakrishnan, A., Lajoie, C.-P., et al. 2014, Proc. SPIE, 9143, 91433X
Rieke, G. H., Wright, G. S., Böker, T., et al. 2015, PASP, 127, 584
Rieke, M. J., Baum, S. A., Beichman, C. A., et al. 2003, Proc. SPIE, 4850, 478
Rieke, M. J., Kelly, D., & Horner, S. 2005, Proc. SPIE, 5904, 1
Rieke, M. J., Kelly, D. M., Misselt, K., et al. 2022, arXiv:2212.12069
Rigby, J., Perrin, M., McElwain, M., et al. 2022, arXiv:2207.05632
Schlawin, E., Leisenring, J., Misselt, K., et al. 2020, AJ, 160, 231
Sérsic, J. L. 1963, BAAA, 6, 41
Sérsic, J. L. 1968, Atlas de Galaxias Australes (Cordoba: Observatorio Astronomico)
Somerville, R. S., & Kolatt, T. S. 1999, MNRAS, 305, 1
Somerville, R. S., Olsen, C., Yung, L. Y. A., et al. 2021, MNRAS, 502, 4858
Somerville, R. S., Popping, G., & Trager, S. C. 2015, MNRAS, 453, 4337
Stefanon, M., Yan, H., Mobasher, B., et al. 2017, ApJS, 229, 32
Virtanen, P., Gommers, R., Oliphant, T. E., et al. 2020, NatMe, 17, 261
Whitaker, K. E., Labbé, I., van Dokkum, P. G., et al. 2011, ApJ, 735, 86
Wright, G. S., Wright, D., Goodson, G. B., et al. 2015, PASP, 127, 595
Yung, L. Y. A., Somerville, R. S., Ferguson, H. C., et al. 2022, MNRAS, 515, 5416
Yung, L. Y. A., Somerville, R. S., Finkelstein, S. L., et al. 2020a, MNRAS, 496, 4574
Yung, L. Y. A., Somerville, R. S., Finkelstein, S. L., et al. 2021, MNRAS, 508, 2706
Yung, L. Y. A., Somerville, R. S., Finkelstein, S. L., Popping, G., & Davé, R. 2019a, MNRAS, 483, 2983
Yung, L. Y. A., Somerville, R. S., Popping, G., et al. 2019b, MNRAS, 490, 2855
Yung, L. Y. A., Somerville, R. S., Popping, G., & Finkelstein, S. L. 2020b, MNRAS, 494, 1002
Zavala, J. A., Buat, V., Casey, C. M., et al. 2023, ApJL, 934, L9
Zitrin, A., Labbé, I., Belli, S., et al. 2015, ApJ, 810, L12